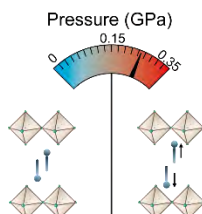


# 5. PRESSURE EFFECTS ON 2D PEROVSKITES



Layered 2D Dion-Jacobson (DJ) and Ruddlesden-Popper (RP) hybrid perovskite are promising materials for optoelectronic applications due to their modular structure. To fully exploit their functionality, mechanical external stimuli could be used to control their properties without changing the composition. However, the responsiveness of these systems to pressure compatible with practical applications ( $< 1$  GPa) remains underexplored. We use hydrostatic pressure to investigate the structure-property relationships in representative iodide and bromide DJ and RP 2D perovskites based on 1,4-phenylenedimethylammonium (PDMA) and benzylammonium (BN) spacers in the 0–0.35 GPa pressure range. Pressure-dependent X-ray diffraction measurements reveal that lattices of these compositions monotonically shrink and DFT calculations provide insights into the structural changes within the organic spacer layer. These structural changes significantly affect the optical properties; the most significant shift in the optical absorption is observed in  $(\text{BN})_2\text{PbBr}_4$  under 0.35 GPa pressure, which is attributed to an isostructural phase transition. Surprisingly, the RP and DJ perovskites behave similarly under pressure, despite the different binding mode of the spacer molecules. This study provides important insights into understanding how the manipulation of the crystal structure affects the optical properties of such materials, whereas the reversibility of their response expands the perspectives for future applications.

*This chapter is based on the following work:*

L. A. Muscarella, A. Dučinskas, M. Dankl, M. Andrzejewski, N. P. M. Casati, U. Rothlisberger, D. Moia, J. Maier, M. Graetzel, B. Ehrler, J. Milic, Reversible Pressure-Dependent Mechanochromism of Dion-Jacobson and Ruddlesden-Popper Layered Hybrid Perovskites, *submitted*

## 5.1. Introduction

Layered two-dimensional (2D) hybrid perovskites have been briefly introduced in **Chapter 1.1**. These materials have attracted considerable interest due to their unique optoelectronic properties and highly modular structure that can be tailored by altering both organic and inorganic components.<sup>1-4</sup> These materials are composed of organic spacer (S) layers connecting adjacent perovskite slabs consisting of  $n$  layers of 3D perovskite based on the  $S_xA_{n-1}M_nX_{3n+1}$  formula that involves a central (A) cation (*e.g.* Cs<sup>+</sup>, methylammonium (MA<sup>+</sup>), formamidinium (FA<sup>+</sup>), etc.) embedded in the {MX<sub>6</sub>} octahedral metal-halide framework based on divalent metal ions (Pb<sup>2+</sup> or Sn<sup>2+</sup>) and halide (X<sup>-</sup>) anions (I<sup>-</sup>, Br<sup>-</sup>, or Cl<sup>-</sup>). They are often broadly classified into Ruddlesden-Popper (RP)<sup>5</sup> and Dion-Jacobson (DJ) phases.<sup>6</sup> In the case of RP perovskites, the perovskite layers are displaced by half the length of the unit cell vectors along the in-plane direction (*a,b*-axis), which mostly involves monofunctional spacers ( $x = 2$ ),<sup>3</sup> whereas DJ perovskites attain the alignment in the structure without relative displacement and are commonly based on bifunctional spacer molecules ( $x = 1$ ; **Figure 5.1a**).<sup>7</sup> They are further classified based on the number of perovskite layers ( $n$ ) which are separated by the organic spacer layer (*e.g.*,  $n = 1, 2, 3$ , etc.).<sup>2,3,8</sup> Since the organic spacers are mostly electronically insulating, the charge carriers in these materials are predominantly confined to the inorganic slabs, resulting in natural quantum well (QW) behaviour (**Figure 5.1b**), where optical bandgaps decrease with the width of the QW because of reduced quantum confinement.<sup>9</sup> This implies that their optical properties can be modulated by changing the number of hybrid perovskite layers ( $n$ ). The QW width and the potential barrier properties, which can be controlled by the spacer size, further affect the optical properties of layered perovskite materials.<sup>10,11</sup>

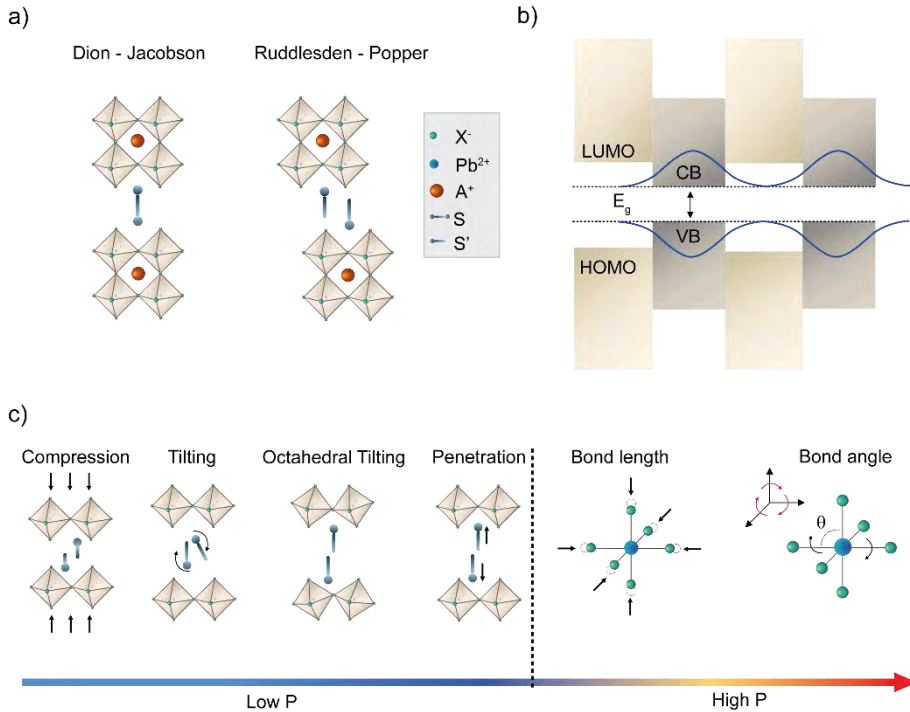


**Figure 5.1.** Layered 2D perovskites and effect of pressure. Schematic representation of **a)** Ruddlesden-Popper and Dion-Jacobson phases and **b)** their quantum well behaviour, with the energy bandgap ( $E_g$ ) defined by conduction band (CB) and valence band (VB) edges of the inorganic slabs and the highest occupied (HOMO) and lowest unoccupied (LUMO) molecular orbitals of the organic spacer layer. In blue, the electronic wavefunction sitting mostly in the inorganic framework and leaking into the organic layers **c)** Illustration of the different structural changes that control the optoelectronic properties of layered hybrid perovskites by external pressure: at low pressures, the main effect is reflected in changes in the organic spacer and octahedral tilting, whereas at high pressures an additional effect on the bond length and angle is expected.

It would be of interest to control these effects on the potential barrier width without changing the perovskite composition, which can be achieved by relying on their mechanical properties and responsiveness to external stimuli, such as pressure.<sup>12,13</sup> Thus, understanding the structure-properties relationship in such

layered perovskites can serve as a guide to design materials with specific optical properties. Simultaneously, knowing the pressure response of these materials opens opportunities for sensing applications, and is important for other applications such as flexible solar cells where strain might be induced during operation.

The relatively low bulk modulus ( $K$ ) of hybrid perovskites (of the order of 10s of GPa) renders them soft materials that are more easily compressible across different pressure ranges, demonstrating mechanochromic behaviour.<sup>14–18</sup> For comparison, halide perovskites show at least a five times smaller bulk modulus than their oxide analogues ( $> 100$  GPa).<sup>19,20</sup> For 2D hybrid halide perovskites, the bulk modulus might not be an appropriate descriptor of their mechanical properties since compression in these materials is mostly anisotropic.<sup>21,22</sup> Alternatively, their mechanical properties can be better described by in-plane or out-of-plane Young's modulus ( $E$ ),<sup>23</sup> which is more commonly used for layered perovskites as it defines the material's ability to deform along a given axis when force is applied along the similar axis. In-plane  $E$  is typically determined by the M–X bond strength, whereas out-of-plane  $E$  depends on the organic spacer.<sup>3,24,25</sup> An appropriate choice of organic spacers can lead to a much smaller  $E$  in the 2D layered perovskites than the 3D analogous,<sup>24,25</sup> suggesting a lower pressure threshold for tuning their optoelectronic and transport properties. The anisotropy of layered hybrid perovskites renders their compression predominant in out-of-plane ( $c$ -axis) direction under mild pressures.<sup>21,22,26</sup> This is expected to be mainly determined by the organic spacer layer and it could result in different structural changes, including the compression of the organic spacer, its tilting, increased penetration depth or octahedral tilting (**Figure 5.1c, left**).<sup>21,22,26</sup> These structural distortions are expected to change the QW structure or the M and X orbital overlaps and, consequently, optical properties. More specifically, the compression of M–X bonds lowers the optical bandgap due to increased antibonding atomic overlap between the metal and halide orbitals, whereas the deviation from the 180° angle (*i.e.* octahedral tilting) leads to an opposite effect.<sup>27</sup> Under higher pressures, the compressed inorganic perovskite lattice relaxes through two competing processes, namely M–X bond tilting or M–X bond

contraction (**Figure 5.1c, right**)<sup>7,28</sup> which directly affect the optoelectronic properties.<sup>12,28</sup>

It is of great importance to study effects in mild pressure regimes ( $< 1$  GPa), since induced levels of strain are comparable with polaron effects,<sup>29,30</sup> chemical (*i.e.* conformational) strain<sup>31,32</sup> or strain due to lattice mismatches,<sup>32,33</sup> especially in 2D/3D perovskite composites.<sup>34</sup> In that regard, the behaviour under mild pressure may serve as a powerful tool for controlling the properties of these materials in a manner comparable to other processes inducing internal strain. However, the investigations of layered hybrid perovskites in such mild-pressure ranges are underrepresented and the differences in the pressure-dependent behaviour of RP and DJ phases remain elusive.

In this Chapter, we investigated representative DJ and RP 2D perovskites based on 1,4-phenylenedimethylammonium (PDMA) and benzylammonium (BN) spacers under hydrostatic pressure up to 0.35 GPa. These aromatic spacer moieties are closely comparable, and they have already demonstrated the capacity to form well-defined 2D perovskite phases,<sup>27,35,36</sup> which makes them appropriate models to analyse the differences in compression between RP and DJ type perovskites. We further study the halide effect on their structure-property relationship by comparing systems based on  $(\text{BN})_2\text{PbX}_4$  and  $(\text{PDMA})\text{PbX}_4$  compositions for  $X = \text{I}, \text{Br}$  halide counter ions by pressure-dependent optical measurements and X-ray diffraction. One would expect that RP layered perovskites are more compressible and more sensitive to external pressure due to Van der Waals interactions in organic bilayer as opposed to DJ. However, we find that the RP and DJ perovskites behave similarly under pressure, despite the different binding mode of the spacer molecules. In addition, we establish no direct pressure-dependent difference between the Br- and I-based compositions and the differences under pressure are more subtle. For all the compositions we observe that the unit cell monotonically shrinks, which is accompanied by a red shift of the optical absorption of the excitonic feature upon increasing the pressure to 0.35 GPa.  $(\text{BN})_2\text{PbBr}_4$  shows the most significant red shift of absorption of the excitonic feature (-54.9 meV) as compared to the other compositions where a comparable shift ( $\sim -30$  meV) is observed. Density functional theory (DFT) calculations reveal that this is due to the increase in Pb–Br–Pb angle which allows

BN spacers penetrating deeper into the inorganic lattice, translating into a stronger pressure response as compared to its iodide counterpart and the PDMA-based DJ systems.

### 5.2. Pressure-dependent Structural Changes

To gain insights into the pressure response of RP and DJ perovskites, we prepared iodide-based precursor solutions using the monofunctional BN and the bifunctional PDMA as organic spacers.<sup>27,35–38</sup> These aromatic spacers were selected based on their comparable structural features that permit the formation of phase-pure RP and DJ perovskites. While iodide-based 2D layered perovskites have been previously investigated in the GPa pressure range (1–12 GPa),<sup>13,21</sup> pressure studies of the bromide-based analogues are unprecedented. Although less investigated due to their high bandgap energy, a fundamental understanding on the dependence of the mechanical response on the halide species is required for designing materials for new applications.

We therefore fabricated thin films based on (PDMA)PbX<sub>4</sub> and (BN)<sub>2</sub>PbX<sub>4</sub> (X = I, Br) compositions as described in the **Experimental Methods 5.5** section. We focused the analysis on these  $n = 1$  2D systems, since they represent the most well-defined layered structures.<sup>2,3,8</sup> Moreover, understanding the behavior of  $n = 1$  layered perovskites provides a limiting case for the analysis of  $n > 1$  systems in the future. The monofunctional spacers in RP phases form bilayers interacting via van der Waals interactions,<sup>39</sup> whereas bifunctional spacers in DJ layered perovskites directly connect the neighbouring perovskite slabs.<sup>40</sup> Accordingly, one might expect that the additional degrees of freedom in RP spacer layers would render them more compressible as compared to their DJ analogues. Similarly, the differences in the lattice parameters of iodide and bromide systems are expected to become apparent in their different behavior under pressure.<sup>41</sup>

Layered perovskite structure in the given thin films is confirmed by well-defined periodic diffraction patterns measured by X-ray diffraction (XRD) at ambient pressure, which exhibit the most intense basal plane reflections below 10° that are followed by higher-order reflections at the higher angles (**Figure 5.2**).

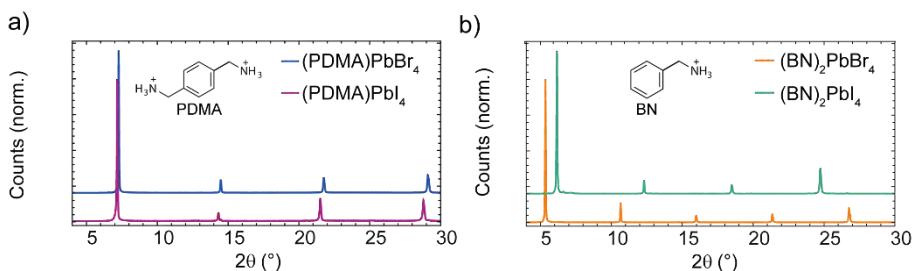


**Figure 5.2.** Structural differences of layered 2D perovskites with bromide and iodide forming the inorganic framework. X-Ray diffraction (Cu K $\alpha$  1.5406 Å) pattern at ambient pressure of **a)** (PDMA)PbX<sub>4</sub> and **b)** (BN)<sub>2</sub>PbX<sub>4</sub> showing a compression of the unit cell for the PDMA-based systems when the iodide counter ion is replaced with the bromide. The opposite is observed for the BN-systems, where the presence of the bromide in the inorganic framework results in the expansion of the unit cell.

A shift towards higher angles is observed when the iodide in the PDMA-based system is replaced by the bromide (**Figure 5.2a**), in accordance with the smaller halide radius which in turn lead to smaller unit cell. On the contrary, when the iodide is replaced by bromide in the BN-based system, we observe the opposite behavior and a shift toward lower angles, indicating a larger unit cell (**Figure 5.2b**). This could suggest a difference in the packing of the spacer for different halide counter ions.

To understand this peculiar behaviour as a function of halide counter ion and to elucidate the role of the physical pressure on the structural properties of these compositions, we investigated pressure-induced changes in the lattice parameters by pressure-dependent X-ray diffraction. Diffraction data of powders for each composition were acquired using a synchrotron source at several pressure points by using a membrane diamond-anvil cell (see **Experimental Methods 5.5** and **Appendix 5.6.3** for details and the attribution of the diffraction peaks). At low pressures, the monoclinic  $P2_1/c$  space group is assigned to (PDMA)PbI<sub>4</sub> and (PDMA)PbBr<sub>4</sub>, the orthorhombic  $Pnma$  to (BN)<sub>2</sub>PbI<sub>4</sub> and the orthorhombic  $Cmc2_1$  to (BN)<sub>2</sub>PbBr<sub>4</sub>. Despite a compression along all the axes (**Figure 5.3a**), the largest compression is recorded along the  $c$ -axis for all systems, which is in

## 5 - Pressure effects on 2D Perovskites

accordance with previous reports<sup>21,26</sup>. This trend is significantly more pronounced for the  $(\text{BN})_2\text{PbBr}_4$  case (**Figure 5.3b**), which shows a larger compression in the out-of-plane  $c$ -axis direction (-8% relative change) and an elongation of the in-plane  $a$  and  $b$  axis followed by a compression (**Figure A5.1** for absolute values of the lattice parameters).

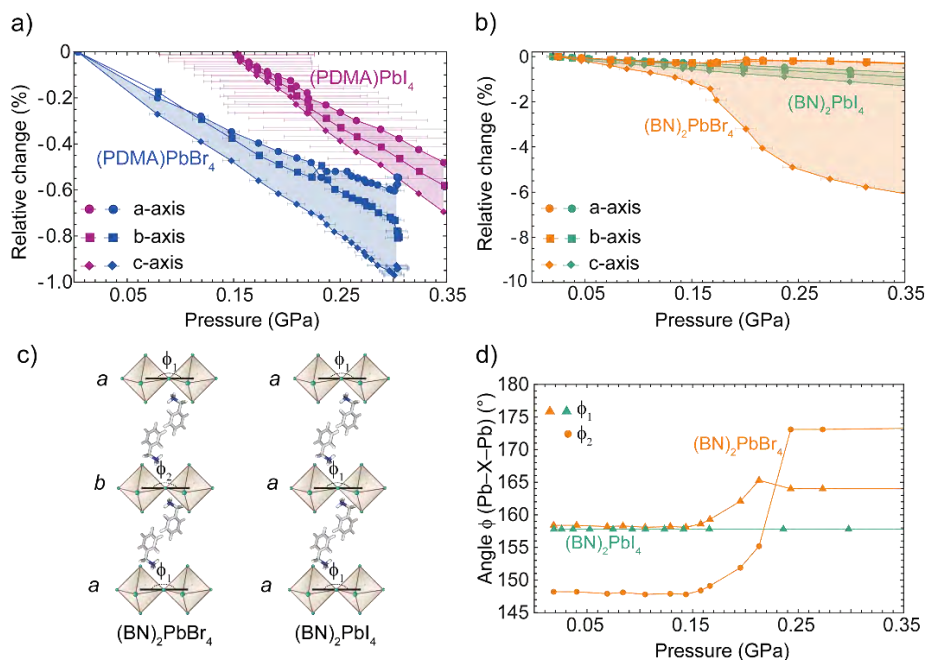


**Figure 5.3.** Pressure-dependent X-ray diffraction with synchrotron source reveal the changes of the inorganic framework as a function of pressure. **a)** Relative change of the lattice parameters as a function of pressure for  $(\text{PDMA})\text{PbX}_4$  and **b)**  $(\text{BN})_2\text{PbX}_4$  compositions. **c)** Schematic representation of  $(\text{BN})_2\text{PbBr}_4$  alternating inorganic sheet ( $aba$ ) in comparison with its iodide counterpart ( $aaa$ ) and the corresponding **d)** inter-octahedral tilting angles in  $(\text{BN})_2\text{PbBr}_4$  and  $(\text{BN})_2\text{PbI}_4$ .

Further structural analysis reveals that there are two distinct values of Pb-X-Pb angles ( $\phi_1$  and  $\phi_2$ ) in  $(\text{BN})_2\text{PbBr}_4$  as compared to  $(\text{BN})_2\text{PbI}_4$ , where only one value of the Pb-X-Pb angle ( $\phi_1$ ) is found (**Figure 5.3c**). Under pressure the angle between two adjacent octahedra hardly changes in the case of  $(\text{BN})_2\text{PbI}_4$ , whereas

the two Pb–Br–Pb angles in (BN)<sub>2</sub>PbBr<sub>4</sub> both change significantly between 0.15 – 0.20 GPa, the range where also the compression along the *c*-axis is strongest (**Figure 5.3d**). Although these changes are remarkable, the *Cmc*<sub>21</sub> space group is maintained, meaning that (BN)<sub>2</sub>PbBr<sub>4</sub> undergoes an isostructural phase transition in this pressure range.<sup>42</sup> Furthermore, to quantify at a first approximation the compressibility of the compositions in study, we calculate the isothermal bulk modulus from the pressure-volume relationship assuming mostly isotropic response to pressure by relying on the second order Birch-Murnaghan equation of state (**Appendix 5.6.4**).<sup>43</sup> Two distinct bulk modulus for (BN)<sub>2</sub>PbBr<sub>4</sub> composition have been identified, which are attributed to low pressure and elevated pressure isostructural phases.<sup>44</sup> In addition, smaller bulk modulus obtained for (BN)<sub>2</sub>PbBr<sub>4</sub> supports its higher susceptibility to compression.

### 5.3. Local Orientation of The Organic Spacer

Since elucidating the local orientation of the organic spacer molecules remains challenging based on the diffraction experiments, we further investigate the effect of pressure on the organic spacer layer by density functional theory (DFT) calculations. To better account for the thermal expansion of the lattice parameters at the measured temperature, the initial structures obtained from the XRD were relaxed while keeping the cell fixed at the experimentally measured values. The results suggest that the compression along the *c*-axis is due to reduced distance between the two neighboring spacers and their closer packing (**Figure 5.4a**). The initial vertical distance between the two BN spacers, *d*(BN-BN), defined from the center of the benzyl ring, is significantly larger in the case of (BN)<sub>2</sub>PbBr<sub>4</sub> (4.43 Å) as compared to (BN)<sub>2</sub>PbI<sub>4</sub> (2.97 Å; **Figure 5.4a**). This distance decreases by 0.4 Å for (BN)<sub>2</sub>PbBr<sub>4</sub>, whereas for the I-based analogue the decrease accounts to only 0.08 Å within the same pressure range, resulting in a larger compression for (BN)<sub>2</sub>PbBr<sub>4</sub> (**Figure 5.4a**). In accordance with the experimental analysis, DFT calculations reveal the presence of two distinct octahedra tilting angles (calculated to be 141.5° and 154.5°) in (BN)<sub>2</sub>PbBr<sub>4</sub> (**Figure 5.4b**). These angles are significantly lower than the one in (BN)<sub>2</sub>PbI<sub>4</sub> (by 4° and 16°, respectively), which leads to higher distortion of the octahedra,

thereby leaving less space for the BN spacers to penetrate. The Pb–X–Pb angles in  $(\text{BN})_2\text{PbBr}_4$  were found to increase with pressure (**Figure 5.4b**), leading to higher penetration depth of the spacers in the inorganic framework (**Figure 5.4c**). This is in contrast with the comparable octahedral tilting in  $(\text{BN})_2\text{PbI}_4$  and in PDMA-based systems (**Figure A5.2a**). In addition, the penetration depth of the spacer in the inorganic framework for the other compositions changes continuously upon increasing pressure (**Figure A5.2b**). The difference in the BN-based systems could thus primarily originate from the changes in the orientation of the spacers and the penetration depth<sup>41</sup> into the inorganic framework, which is defined by the distance between the nitrogen atom of the ammonium group of the spacer moiety and the axial halide plane. In addition to the penetration of the spacer layer one might expect also the Pb–X bond length to change under pressure. The equatorial Pb–Br bond lengths in  $(\text{BN})_2\text{PbBr}_4$  at low pressure (2.98 Å and 3.02 Å; **Figure A5.2c**) are smaller than the ones in  $(\text{BN})_2\text{PbI}_4$  (3.21 Å and 3.25 Å; **Figure A5.2c**), leading to a denser octahedral packing and, in turn, a significantly lower penetration into the Pb–Br lattice at ambient pressure. These structural differences in the low-pressure structures also translate into different responses to external pressure. However, the axial Pb–X bond lengths (**Figure A5.2c**) remain constant over the entire pressure range. This implies that the measured compressions are not caused by changes in the bond lengths of Pb–X. Instead, the response to mild pressure is the result to changes in the packing in the organic spacer layer (**Figure A5.3**). While  $(\text{BN})_2\text{PbI}_4$  and  $(\text{PDMA})\text{PbX}_4$  show no significant change, the two BN spacers in  $(\text{BN})_2\text{PbBr}_4$  move closer together (**Table 5.2, Table 5.3, Table 5.4, Table 5.5**). Our calculations reveal that in the pressure range between 0.164 GPa to 0.213 GPa the BN spacers penetrate deeper into the inorganic lattice of  $\text{PbBr}_4$  (**Figure 5.4c**).

### 5.3 - Local Orientation of The Organic Spacer

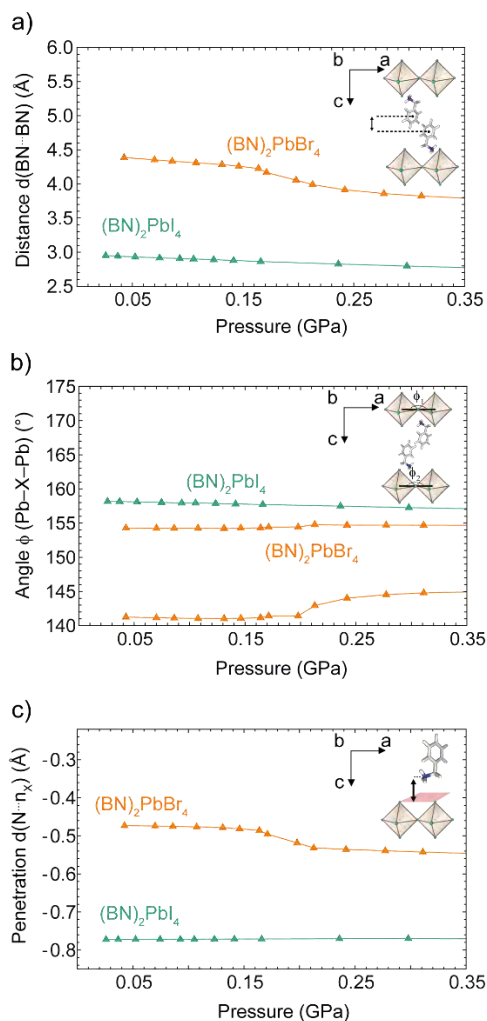


**Figure 5.4.** Calculated location of the organic spacer and interoctahedral angles as a function of pressure. Calculated **a)** average distances of the (vertically) neighboring BN rings  $d(\text{BN}\cdots\text{BN})$  in the RP layer; **b)** average Pb–X–Pb angles in the Pb–X planes  $\phi(\text{Pb-X-Pb})$  as a measure of the equatorial tilting of the octahedra; and **c)** nitrogen penetration depth in the halide plane  $d(\text{N}\cdots n_x)$  as a measure of the penetration depth from DFT optimized structures (PBEsol).

It is important to note that the zero is set at the halide planes and larger penetration corresponds to more negative values. This process is accompanied by

a decrease in the BN tilting angle,  $\phi(\text{BN}\cdots\text{n}_{\text{PbX}})$ , defined as the angle between the *c*-axis and the benzyl plane (**Figure A5.2d**). Such a change corresponds to a rearrangement of the BN spacers into a more parallel orientation with respect to the *c*-axis (**Figure A5.2d**). Consequently, the significant change in the distance between the neighbouring BN groups is in accordance with the experimental observation of a larger compression for  $(\text{BN})_2\text{PbBr}_4$ . Such changes in the assembly of the spacer layer in response to pressure are further reflected in their optical properties.

## 5.4. Pressure-dependent Mechanochromism

To assess the mechanochromic properties, we monitored the optical absorption energy of the excitonic feature as a function of applied external stress by measuring pressure-dependent absorption spectra of  $(\text{PDMA})\text{PbX}_4$  and  $(\text{BN})_2\text{PbX}_4$  ( $X = \text{Br}, \text{I}$ ). The samples were placed inside a hydrostatic pressure cell filled with an inert liquid (tetradecafluorohexane, FC-72, **Experimental Methods 5.5** and schematically depicted in **Figure 5.5a**). We applied pressure from 0 to 0.350 GPa in steps of 0.050 GPa through a manual pump. Quantum and dielectric confinement effects give rise to an intense and narrow excitonic feature (**Figure A5.4**), typical of layered 2D perovskites.<sup>45,46</sup> We observe a continuous shift of the excitonic peak toward lower energies for all analysed layered perovskite compositions (**Figure 5.5b-e**). In addition, the red-shift confirms that a mild external pressure can be sufficient to tune the optical properties in these materials. Similarly, pressure-dependent photoluminescence measurements show a red-shift toward smaller energy upon increasing pressure (**Figure A5.5**). We obtained the excitonic peak energy of the  $(\text{PDMA})\text{PbI}_4$  and  $(\text{BN})_2\text{PbI}_4$  as a function of pressure fitting a skewed Gaussian function to optical spectra measured. At ambient pressure, the excitonic peak energy of  $(\text{PDMA})\text{PbI}_4$  and  $(\text{BN})_2\text{PbI}_4$  is 2.41 eV and 2.36 eV, respectively.

Upon increasing the pressure, the excitonic-peak shift at 0.30 GPa as compared to ambient pressure is about  $(-25 \pm 0.6)$  meV for  $(\text{PDMA})\text{PbI}_4$  and  $(-27 \pm 1)$  meV for  $(\text{BN})_2\text{PbI}_4$  (**Figure 5.5f**). We observed a similar linear trend for both RP and DJ perovskites until 0.30 GPa, where the response to external

## 5.4 - Pressure-dependent Mechanochromism

pressure causes a comparable energy shift. From 0.30 GPa onward, the  $(\text{BN})_2\text{PbI}_4$  appears to shift to a larger extent in comparison with the  $(\text{PDMA})\text{PbI}_4$ , showing an energy shift of  $(-33 \pm 1)$  meV and  $(-27 \pm 0.5)$  meV, respectively.

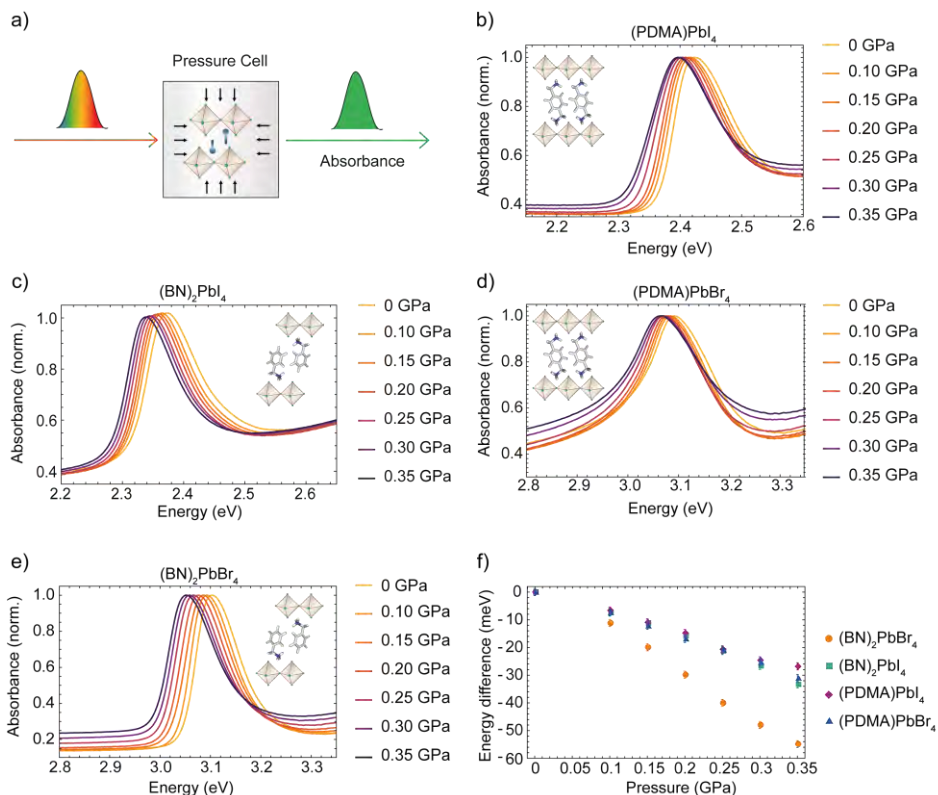


**Figure 5.5.** Optical measurements reveal a red-shift of the excitonic feature. Schematic of the **a)** experimental setup for pressure-dependent absorption measurements and **b)** pressure-dependent absorbance collected  $(\text{PDMA})\text{PbI}_4$ , **c)**  $(\text{BN})_2\text{PbI}_4$ , **d)**  $(\text{PDMA})\text{PbBr}_4$  and **e)**  $(\text{BN})_2\text{PbBr}_4$  from ambient to 0.35 GPa. The inset shows a schematic representation of the layered structures. **f)** Energy difference of the excitonic peak energy as a function of applied pressure.

Further investigations at pressures above 0.35 GPa are not possible with the same experimental setup because of the limitations of the windows of the hydrostatic pressure cell. Moreover, monitoring the shift of the excitonic peak by its maximum intensity reveals the same slope as fitting the skewed Gaussian with a

larger error given by the resolution of the measurement (**Figure A5.6** and **Table 5.6, Table 5.7, Table 5.8, Table 5.9**). Considering the bromide analogues, the excitonic peak energy is 3.06 eV and 3.07 eV for (PDMA)PbBr<sub>4</sub> and (BN)<sub>2</sub>PbBr<sub>4</sub>, respectively. Upon increasing the pressure from ambient to 0.35 GPa, the energy shifts for both (PDMA)PbBr<sub>4</sub> and (BN)<sub>2</sub>PbBr<sub>4</sub> by  $(-31 \pm 1)$  meV and  $(-55 \pm 0.2)$  meV, respectively. The (BN)<sub>2</sub>PbBr<sub>4</sub> perovskite, despite showing a red-shift as a function pressure, has a notably larger energy shift than its iodide counterpart and the PDMA-based systems (**Figure 5.5f** and **Table 5.6, Table 5.7, Table 5.8** and **Table 5.9**). To sum up, the energy shifts in iodide-based samples are closely corresponding to each other, which suggest that pressure-dependent properties are comparable for RP and DJ phases. However, bromide-based systems show contrasting differences, with (BN)<sub>2</sub>PbBr<sub>4</sub> having remarkably larger shifts than (PDMA)PbBr<sub>4</sub> and the I-based systems.

The expected change in the bandgap was calculated for all the compositions by DFT (**Figure A5.7, Table 5.10, Table 5.11,**

**Table 5.12, Table 5.13**) to observe qualitative variations of the bandgaps as a function of pressure, which corroborate with the experimental results. The larger red shift in (BN)<sub>2</sub>PbBr<sub>4</sub> is in accordance with the significantly larger compressibility of (BN)<sub>2</sub>PbBr<sub>4</sub> as compared to its iodide-based analogue and the PDMA-based systems (**Figure A5.10**). Furthermore, the isostructural phase transition induced by the reduction of octahedral tilting (*i.e.* the Pb–Br–Pb tilting is closer to 180° at the highest pressure measured) is associated with the change of penetration depth of the BN spacers into the perovskite lattice, which in turn favours a larger red shift of the optical absorption. Finally, we can directly correlate the experimental structural parameters obtained by pressure-dependent XRD measurements with the change in the optical absorption.

The relationship between the shift in the exciton absorption peak and the length of the *c-axis* is linear for both PDMA-based and BN-based samples (**Figure 5.6a,b**), with the exception in (BN)<sub>2</sub>PbBr<sub>4</sub>, where we observe two different regimes which attributed to the isostructural phase transition.

## 5.4 - Pressure-dependent Mechanochromism

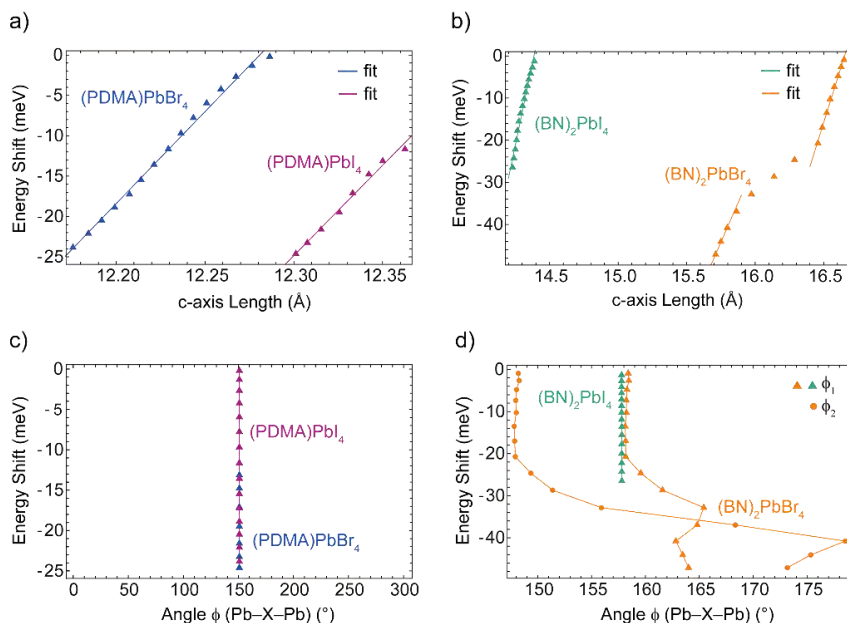


**Figure 5.6.** Optical properties dependency on the compression of the  $c$ -axis and interoctahedral angles. Optical absorption shift in meV as a function of **a)** the  $c$ -axis length for PDMA-systems and **b)** BN-systems, and as a function of the Pb–X–Pb angles for **c)** for PDMA-systems and **d)** BN-systems based on the experimental data.

A linear fit of the energy shift as a function of the  $c$ -axis length results in a slope of  $0.227 \text{ eV}/\text{\AA}$ ,  $0.223 \text{ eV}/\text{\AA}$  for (PDMA) and  $\text{PbBr}_4$  (PDMA) $\text{PbI}_4$ , respectively. We obtain a slope of  $0.156 \text{ eV}/\text{\AA}$  for  $(\text{BN})_2\text{PbI}_4$ ,  $0.104 \text{ eV}/\text{\AA}$  and  $0.074 \text{ eV}/\text{\AA}$  for  $(\text{BN})_2\text{PbBr}_4$  below and above the isostructural phase transition, respectively (**Figure 5.6a,b**). This finding suggests a larger dependency of the PDMA systems on the change of the  $c$ -axis compared to the BN systems. No correlation is observed between Pb–X–Pb angle and the optical properties (**Figure 5.6c,d**), except in the case of isostructural phase transition regime in  $(\text{BN})_2\text{PbBr}_4$  (**Figure 5.6d**). Thus, we find that in the representative DJ and RP layered 2D perovskites presented in this study, the bandgap change is largely caused by the compression of the  $c$ -axis which is expected because of the reduced quantum confinement but no correlation is found with the Pb–X–Pb angles within the same structural phase.

## 5 - Pressure effects on 2D Perovskites

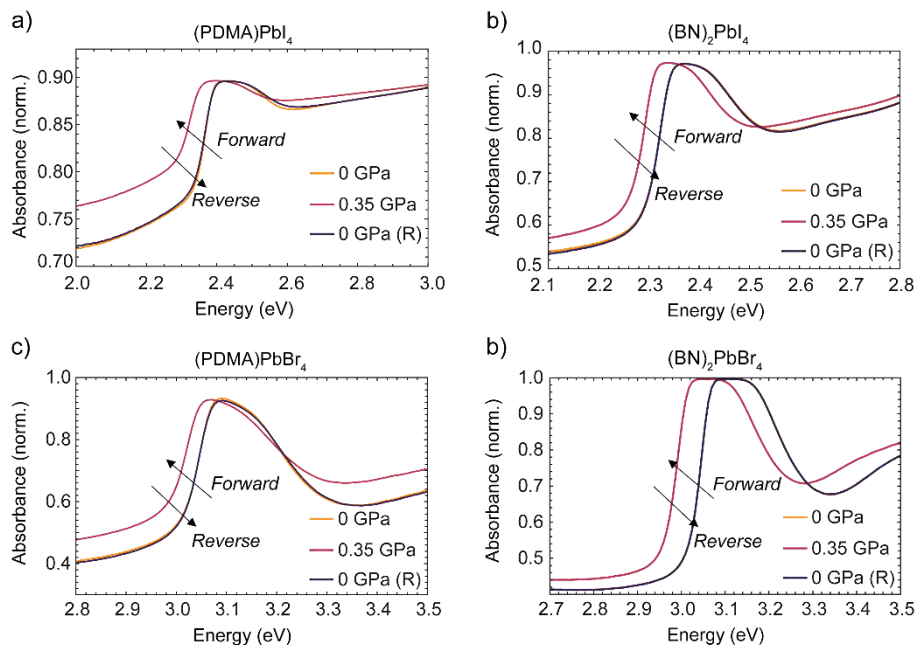


**Figure 5.7.** Fully reversible mechanochromism. Pressure-dependent absorption recorded at three characteristic pressures in the upward and downward direction for **a)** (PDMA)PbI<sub>4</sub> and **b)** (BN)<sub>2</sub>PbI<sub>4</sub>, **c)** (PDMA)PbBr<sub>4</sub> and **d)** (BN)<sub>2</sub>PbBr<sub>4</sub>.

The shift of the excitonic peak is fully recovered for both I<sup>-</sup> and Br<sup>-</sup> based RP and DJ perovskite samples upon decompression from 0.35 GPa to ambient pressure, implying that the process is reversible in this pressure range. The corresponding absorption spectra of both materials almost perfectly overlap in shape and intensity after decompression (**Figure 5.7**). The reversibility of the optical features strongly suggests structural reversibility, which is in agreement with the DFT predictions and in contrast with the amorphization commonly reported at higher pressures.<sup>47–49</sup> This reversibility of the mechanochromic response of layered hybrid perovskites is of interest to their use as model systems for elucidating structure-property relationships in hybrid layered materials, provides promise for the long-term stability of flexible perovskite devices, but also points towards the use of mechanophores in the development of various smart materials and pressure sensors.<sup>50–52</sup>

## 5.4. Conclusion

In summary, we reported a direct comparison of the response of iodide and bromide-based RP and DJ 2D perovskites to pressure by using comparable aromatic spacer moieties, namely benzylammonium (BN) and 1,4-phenylenedimethylammonium (PDMA), respectively. We applied a mild pressure up to 0.35 GPa to all the compositions and detected a red shift of the excitonic peak upon increasing the pressure. Whereas PDMA-based DJ perovskites were not found to be susceptible to changes associated with the halide ion, BN-based perovskite results in a larger shift of the optical absorption associated with the excitonic feature in bromide-based compositions that is in contrast with their higher expected level of rigidity. Furthermore, X-ray diffraction experiments in conjunction with DFT calculations under pressure suggest that this effect is related to the structural properties of the 2D perovskite phases. Specifically, X-ray diffraction experiments reveal the presence of an isostructural phase transition in  $(\text{BN})_2\text{PbBr}_4$  that maintain the orthorhombic  $Cmc2_1$  space group, whereas no phase transition is detected for the other compositions. DFT computations further indicate that this isostructural space group transition is associated with a decrease in the octahedra tilting which leads to an increased penetration depth of the BN spacers into the Pb–Br lattice. These changes explain the large compression of  $(\text{BN})_2\text{PbBr}_4$  under mild pressures up to 0.350 GPa. This study thereby provides important insights into the mechanochromic properties of layered hybrid perovskites. Finally, the unique reversibility of their mechanochromic response in this mild pressure range opens new perspective towards the utility of layered hybrid perovskites as platforms for amphotodynamic materials<sup>53,54</sup> and mechanophores,<sup>50-52</sup> which expands the perspectives for their future applications.

## 5.5. Experimental Methods

### Sample Preparation

Iodide-based solutions were obtained mixing  $\text{PbI}_2$  and  $(\text{PDMA})\text{I}_2$  powders in 1:1 stoichiometric ratio for  $(\text{PDMA})\text{PbI}_4$ , whereas 1:2 ratio of  $\text{PbI}_2:(\text{BN})\text{I}$  for  $(\text{BN})_2\text{PbI}_4$ . Subsequently, solid mixtures were dissolved in the *N,N*-dimethylformamide (DMF) and dimethyl sulfoxide (DMSO) solvent mixture (4:1, v/v) to obtain 0.2 M solution. Bromide-based solutions were made mixing  $\text{PbBr}_2:(\text{PDMA})\text{Br}_2$  in 1:1 ratio for  $(\text{PDMA})\text{PbBr}_4$  and in 1:2  $\text{PbBr}_2:(\text{BN})\text{Br}$  for  $(\text{BN})_2\text{PbBr}_4$ . The mixtures were then dissolved in (DMF:DMSO) (1:1, v/v) solvent to obtain 0.2 M solution. All the films were solution-processed by spin-coating. Before deposition, the glass substrates were ultrasonically cleaned with acetone and ethanol sequentially for 5 min, followed by UV-Ozone cleaning/treatment for 15 min. Precursor solution was dropped on the glass substrate (Assitent 50), which was afterwards spun at 1000 rpm and 4000 rpm for 10 s and 20 s, respectively. Spin-coated films were annealed on a hot plate at 150 °C for 10 min. Solution preparation was carried out in an argon atmosphere glovebox ( $0.5 \text{ ppm} < \text{O}_2$  and  $0.5 \text{ ppm} < \text{H}_2\text{O}$ ), whereas sample deposition in the dry air glovebox ( $RH \approx 5\%$ ). Perovskite powders were prepared using mechanosynthesis by grinding in a ball mill (Retsch Ball Mill MM-200) using a grinding jar (10 ml) and a ball ( $\varnothing 10 \text{ mm}$ ) for 30 min at 25 Hz. The molar ratios of all the precursors were stoichiometric and the resulting powders were annealed at 150 °C for 30 min.

### Pressure-dependent absorption

We measured pressure-dependent absorption using a LAMBDA 750 UV/Vis/NIR Spectrophotometer (Perkin Elmer). The samples are placed inside a pressure cell (ISS Inc.) filled with inert liquid (perfluorohexane, FC-72, 3M). The increase in the volume of the liquid inside the pressure cell upon pumping generates high pressure. Measurements are performed from ambient pressure to 0.350 GPa, in steps of 0.050 GPa, and we waited 7 min before measuring at each pressure to ensure equilibration under pressure. Prior to use, the liquid is degassed in a Schlenk line to remove oxygen, responsible for scattering of light above 0.3

GPa and consequent reduction of the transmitted signal. We estimate an error of the reading of 0.020 GPa.

### **X-Ray Diffraction**

Measurements of perovskite thin films were carried out using PANalytical Empyrean Series 2 instrument in Bragg-Brentano configuration with Cu K $\alpha$  radiation at 40 kV voltage and 40 mA current. A nickel filter was used to reduce K $\beta$  contribution. X-rays were detected using a PIXcel3d detector.

### **Steady-State Photoluminescence**

We measured photoluminescence (PL) with a home-built setup equipped with a 405 nm CW laser source (S1FC405, Thorlabs) for the iodide-based perovskite composition (PDMA-I and BN-I). The PL was coupled into a fiber connected to an OceanOptics USB4000 spectrometer. To remove the excitation laser from the acquired signal, a long-pass filter LP500 was mounted before the spectrometer. An integration time of 1 second was used for each measurement. To measure the PL of bromide-based perovskite composition (PDMA-Br and BN-Br), a 375 nm laser was used.

### **Density Functional Theory**

All computations were done on the DFT level of theory with the software package Quantum ESPRESSO v6.6 using ultrasoft pseudopotentials from the pslibrary 1.0.0, a wavefunction cutoff of 60 Ry, a charge density cutoff of 480 Ry, Gaussian spreading of 0.005 Ry and the semiempirical Grimme's DFT-D3 vdW correction.<sup>55-57</sup> Relaxations were performed using the PBEsol functional in which the energies and forces are converged up to  $10^{-7}$  Ry and  $10^{-6}$  Ry/Bohr, respectively, with the system specific converged at  $\Gamma$ -point centered k-point Monkhorst-Pack grid (**Table 5.1**). For the computations of the bandgap, single point energy computations were done on the relaxed structures using the Perdew-Burke-Ernzerhof (PBE) functional with a wavefunction convergence up to  $10^{-8}$  Ry and (apart from (BN)<sub>2</sub>PbBr<sub>4</sub>) at higher k-point Monkhorst-Pack grid (**Table 5.1**). For each pressure, the experimentally obtained structure files are taken and

used for relaxation while keeping the cell fixed. For the PDMA based systems, a  $2 \times 2 \times 1$  supercell was created prior to relaxation.

**Table 5.1.** *k*-point Monkhorst-Pack grid used for the relaxation and SPE of the systems.

System	Relaxation	SPE
(BN) <sub>2</sub> PbBr <sub>4</sub>	8×8×2	8×8×2
(BN) <sub>2</sub> PbI <sub>4</sub>	6×6×2	9×10×3
(PDMA)PbX <sub>4</sub> (X=Br,I)	4×4×6	6×6×9

### High-pressure powder X-Ray diffraction

High-pressure powder X-ray diffraction measurements were performed with synchrotron radiation in the Swiss Light Source ( $\lambda = 0.49217 \text{ \AA}$  and Pilatus 6M detector).<sup>58</sup> The samples were compressed in a membrane diamond-anvil cell using DAPHNA oil as medium. Prior to the measurement, the cell is pre-pressurized applying a pressure of 3-4 bars on the membrane to avoid leaks and ensure a good sealing of the cell. This results in a slightly higher value for the first datapoint with respect to ambient pressure. We note that the response of the membrane used to measure the (PDMA)PbBr<sub>4</sub> is higher than for the other compositions, resulting in higher starting pressure. We used  $\alpha$ -quartz as a pressure calibrant, blended with a sample, and diffraction patterns of the mixture were collected. The equation of state of quartz was used to determine pressure with accuracy of approximately 0.005 GPa.<sup>59</sup> Raw data was processed in Dioptas<sup>60</sup> extracting patterns of the mixtures after masking diffraction spots from the diamonds. PXRD patterns were treated with TOPAS software and unit-cell parameters were determined using Rietveld refinement.<sup>61,62</sup>

## 5.6. Appendix

### 5.6.1. ADDITIONAL FIGURES

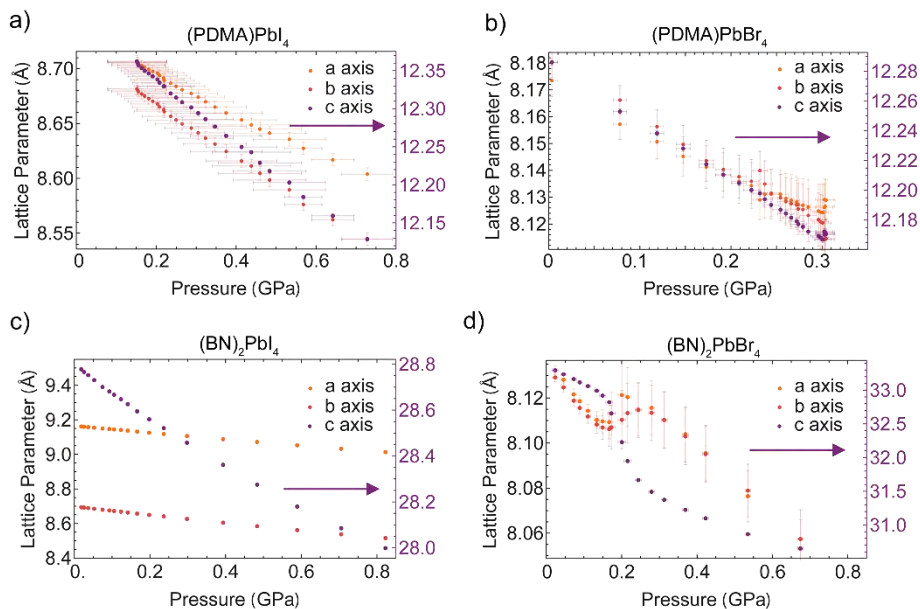


**Figure A5.1.** Lattice parameters as a function of pressure obtained from Rietveld refinements of diffraction patterns for **a)** (PDMA)PbI<sub>4</sub>, **b)** (BN)<sub>2</sub>PbI<sub>4</sub>, **c)** (PDMA)PbBr<sub>4</sub>, **d)** (BN)<sub>2</sub>PbBr<sub>4</sub>. The right axis refers to the *c*-axis (in purple).

## 5 - Pressure effects on 2D Perovskites

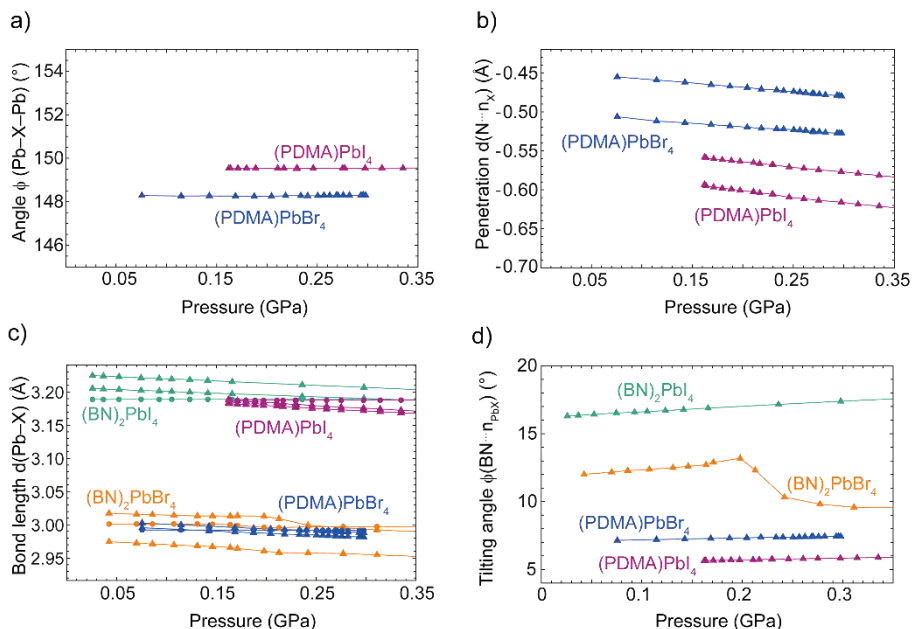


**Figure A5.2.** Computed **a)**  $\phi(Pb-X-Pb)$  tilting angle and **b)** nitrogen penetration depth in the plane formed by the halide atoms  $d(N\cdots n_X)$ . The penetration depths of the two nitrogen in the PDMA spacer are not equivalent. Computed **c)** average equatorial (triangle) and axial (disk) Pb–X bond lengths  $d(Pb-X)$ . The octahedra has two inequivalent equatorial bonds and one axial bond and **d)** average tilting angles of the benzyl ring relative to the *c*-axis  $\phi(BN\cdots n_{PbX})$ .

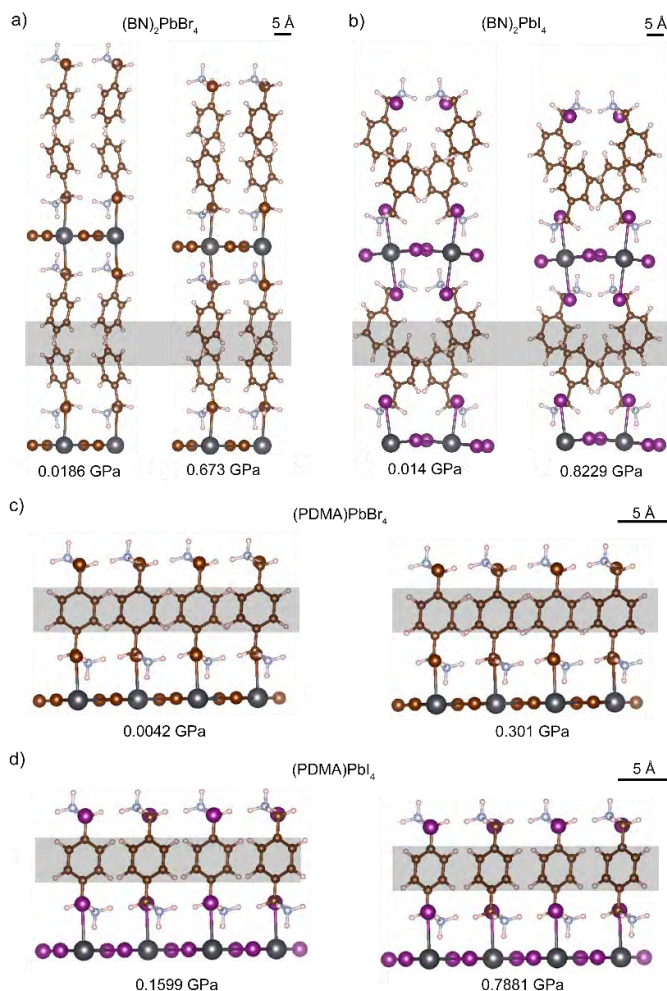


**Figure A5.3.** Relaxed structures of **a)**  $(\text{BN})_2\text{PbBr}_4$  at 0.014 GPa and at 0.673 GPa, **b)**  $(\text{BN})_2\text{PbI}_4$  at 0.0186 GPa and at 0.8229 GPa. **c)**  $(\text{PDMA})\text{PbBr}_4$  at 0.0042 GPa and at 0.3011 GPa, **d)**  $(\text{PDMA})\text{PbI}_4$  at 0.1598 GPa and 0.7881 GPa. The rectangle in grey highlights the change in the spacers' distance for all the systems at a representative low and high pressure.

## 5 - Pressure effects on 2D Perovskites

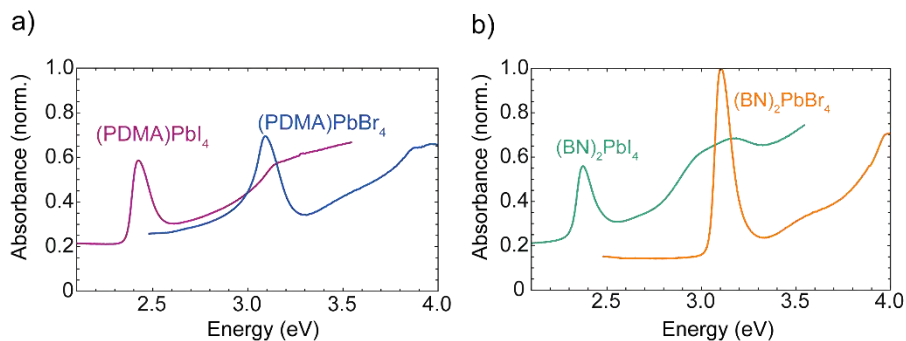


**Figure A5.4.** Normalized absorbance collected at ambient pressure for **a)** (PDMA)PbI<sub>4</sub> and (PDMA)PbBr<sub>4</sub>, **b)** (BN)<sub>2</sub>PbI<sub>4</sub> and (BN)<sub>2</sub>PbBr<sub>4</sub> highlighting the presence of the typical excitonic feature observed in layered 2D perovskites.

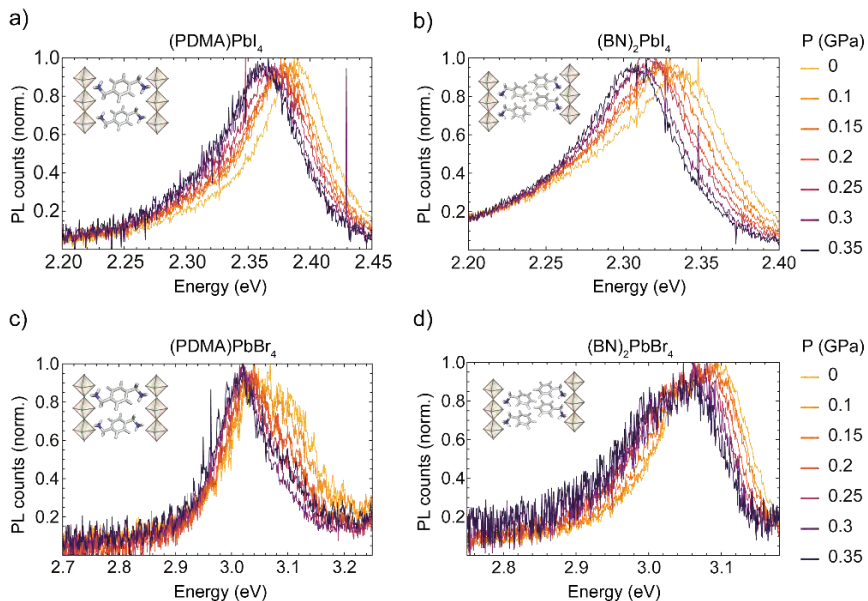


**Figure A5.5.** Pressure-dependent photoluminescence for **a)** (PDMA)PbI<sub>4</sub>, **b)** (BN)<sub>2</sub>PbI<sub>4</sub>, **c)** (PDMA)PbBr<sub>4</sub>, **d)** (BN)<sub>2</sub>PbBr<sub>4</sub>. The photoluminescence peak shifts towards smaller energy as a function of pressure for all the compositions studied.

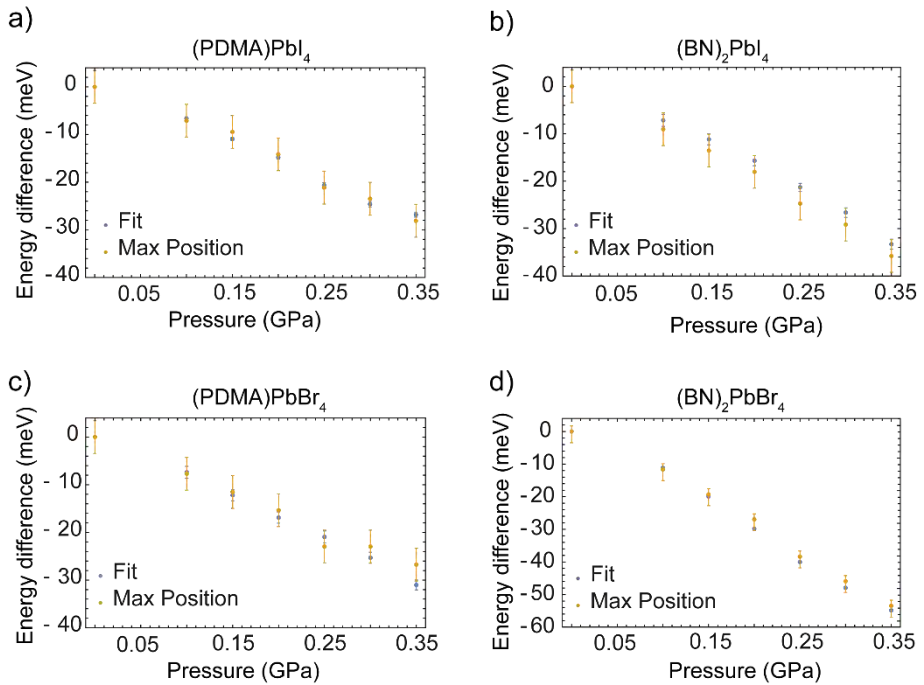


**Figure A5.6.** Excitonic peak estimated using a skewed gaussian fit (blue) and the maximum intensity position of the excitonic feature (in orange) for **a)** (PDMA)PbI<sub>4</sub>, **b)** (BN)<sub>2</sub>PbI<sub>4</sub>, **c)** (PDMA)PbBr<sub>4</sub>, **d)** (BN)<sub>2</sub>PbBr<sub>4</sub>. The two methods result in comparable results. The larger error in the second method is given by the resolution of the measurement.

## 5 - Pressure effects on 2D Perovskites

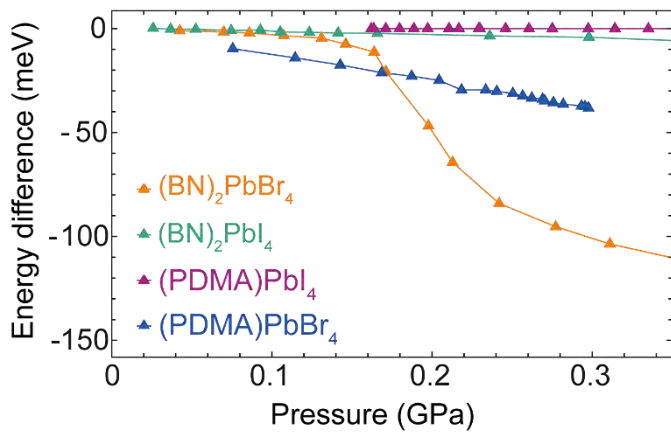


**Figure A5.7.** DFT calculation of the change of bandgap  $E_{\text{gap}}$  relative to the corresponding structure at low pressure for all the compositions in study.

## 5.6.2. ADDITIONAL TABLES

**Table 5.2.** Absolute values of the DFT calculated equatorial and axial bond length  $d(Pb-X)$ , bond angle  $Pb-X-Pb$ , distance from the nitrogen of each organic spacer to the X plane  $d(N\cdots n_X)$ , titing angle between the organic spacer the  $Pb-X$  plane  $\phi(N\cdots Pb-X)$  for (PDMA)PbI<sub>4</sub> as a function of pressure.

<i>Pressure</i> (GPa)	<i>Pb-X-Pb</i> (°)	<i>d(Pb-X)<sub>ax</sub></i> (Å)	<i>d(Pb-X)<sub>eq</sub></i> (Å)	<i>d(N<math>\cdots</math> n<sub>X</sub>)</i> (Å)	<i>d(N<math>\cdots</math> n<sub>X</sub>)</i> (Å)	<i><math>\phi(N\cdots Pb-X)</math></i> (°)
<b>0.1598</b>	149.5329	3.1885	3.18315	-0.5933	-0.55825	5.64388
<b>0.1621</b>	149.5348	3.18812	3.18276	-0.5949	-0.5592	5.65079
<b>0.1636</b>	149.5361	3.18749	3.1823	-0.5965	-0.56033	5.66000
<b>0.1711</b>	149.5376	3.18683	3.18167	-0.5979	-0.56151	5.67174
<b>0.1797</b>	149.5426	3.18606	3.18105	-0.5992	-0.56259	5.68260
<b>0.1887</b>	149.5367	3.1853	3.1803	-0.6007	-0.56374	5.69450
<b>0.1973</b>				-0.6025	-0.56506	5.71414
<b>0.2106</b>	149.5398	3.18369	3.17889	-0.6040	-0.56638	5.71800
<b>0.2168</b>	149.5377	3.18267	3.17802	-0.6056	-0.56783	5.731925
<b>0.2292</b>	149.5198	3.18119	3.17658	-0.6059	-0.56793	5.755073
<b>0.2299</b>	149.5434	3.18185	3.17718	-0.6095	-0.57081	5.746575
<b>0.2459</b>	149.5398	3.17971	3.17529	-0.6113	-0.57254	5.778501
<b>0.2605</b>				-0.6135	-0.5744	5.794679
<b>0.2751</b>	149.5377	3.17726	3.17303	-0.6159	-0.57671	5.816089
<b>0.2975</b>	149.5439	3.17588	3.17175	-0.6185	-0.57908	5.836809
<b>0.3142</b>	149.5448	3.17432	3.1703	-0.6209	-0.58163	5.861448
<b>0.3351</b>	149.547	3.17257	3.16869	-0.6244	-0.58475	5.883516
<b>0.3597</b>	149.5609	3.16817	3.16462	-0.6282	-0.5886	5.916929
<b>0.3934</b>	149.5703	3.16518	3.16196	-0.6327	-0.59339	5.953579
<b>0.4299</b>				-0.6344	-0.59578	5.999345
<b>0.4576</b>				-0.6398	-0.6000	6.021744
<b>0.4838</b>				-0.6428	-0.60357	6.066036
<b>0.5085</b>	149.6319	3.15907	3.15646	-0.6475	-0.60857	6.100086
<b>0.5515</b>	149.638	3.15629	3.15385	-0.6539	-0.61504	6.142101
<b>0.5994</b>	149.6621	3.15251	3.1504	-0.6614	-0.62352	6.207654
<b>0.6734</b>				-0.6716	-0.6336	6.295497
<b>0.7881</b>					-0.5582	6.378513

## 5 - Pressure effects on 2D Perovskites

**Table 5.3.** Absolute values of the DFT calculated equatorial and axial bond length  $d(Pb-X)$ , bond angle  $Pb-X-Pb$ , distance from the nitrogen of each organic spacer to the X plane  $d(N\cdots n_X)$ , titing angle between the organic spacer the  $Pb-X$  plane  $\phi(N\cdots Pb-X)$  for (PDMA)PbBr<sub>4</sub> as a function of pressure.

<i>Pressure</i> (GPa)	<i>Pb-X-Pb</i> (°)	<i>d(Pb-X)<sub>ax</sub></i> (Å)	<i>d(Pb-X)<sub>eq</sub></i> (Å)	<i>d(N<math>\cdots</math> n<sub>X</sub>)</i> (Å)	<i>d(N<math>\cdots</math> n<sub>X</sub>)</i> (Å)	<i><math>\phi(N\cdots Pb-X)</math></i> (°)
<b>0.0042</b>	148.2977	3.0086	3.00124			
<b>0.0756</b>	148.2827	3.002715	2.99565	-0.50629	-0.45516	7.024311
<b>0.1146</b>	148.266	2.99997	2.99308	-0.51182	-0.45921	7.146059
<b>0.1427</b>	148.2715	2.997863	2.99308	-0.51397	-0.4620	7.203226
<b>0.1686</b>	148.2562	2.996003	2.98911	-0.51635	-0.46520	7.248788
<b>0.1873</b>	148.248	2.994741	2.98797	-0.51803	-0.46714	7.28877
<b>0.2044</b>	148.2498	2.993764	2.98711	-0.5197	-0.46877	7.306107
<b>0.2184</b>	148.2777	2.992746	2.98585	-0.5211	-0.47095	7.33093
<b>0.2335</b>	148.2772	2.992309	2.98547	-0.52171	-0.47203	7.372813
<b>0.2404</b>	148.2706	2.991744	2.98496	-0.52207	-0.47298	7.36974
<b>0.2504</b>	148.2782	2.991343	2.98463	-0.52297	-0.47393	7.373831
<b>0.2566</b>	148.2928	2.990668	2.98457	-0.52350	-0.47460	7.379919
<b>0.2623</b>	148.2872	2.990378	2.98352	-0.52395	-0.47559	7.398313
<b>0.269</b>	148.2957	2.990151	2.9834	-0.52520	-0.47630	7.405101
<b>0.2704</b>	148.2907	2.98981	2.98306	-0.52573	-0.47670	7.410301
<b>0.2758</b>	148.3007	2.989559	2.98281	-0.52556	-0.47733	7.417375
<b>0.2819</b>	148.2979	2.989176	2.98245	-0.52646	-0.47822	7.421604
<b>0.2933</b>	148.2951	2.988621	2.98193	-0.52733	-0.47895	7.430358
<b>0.2955</b>	148.3059	2.988262	2.9815	-0.52748	-0.47934	7.437077
<b>0.2979</b>	148.2996	3.0086	2.98137	-0.52728	-0.4798	7.445589

**Table 5.4.** Absolute values of the DFT calculated equatorial and axial bond length  $d(\text{Pb}-\text{X})$ , bond angle  $\text{Pb}-\text{X}-\text{Pb}$ , distance from the nitrogen of each organic spacer to the X plane  $d(\text{N}\cdots\text{n}_\text{X})$ , titing angle between the organic spacer the  $\text{Pb}-\text{X}$  plane  $\phi(\text{N}\cdots\text{Pb}-\text{X})$  and the distance between the spacer  $d(\text{BN}\cdots\text{BN})$  for  $(\text{BN})_2\text{PbI}_4$  as a function of pressure.

<i>Pressure</i> (GPa)	<i>Pb-X-Pb</i> (°)	<i>d(Pb-X)<sub>ax</sub></i> (Å)	<i>d(Pb-X)<sub>eq</sub></i> (Å)	<i>d(Pb-X)<sub>eq</sub></i> (Å)	<i>d(BN-BN)</i> (Å)	<i>d(N⋯n<sub>X</sub>)</i> (Å)	<i>φ(N⋯Pb-X)</i> (°)
<b>0.0186</b>	158.226	3.188795	3.205568	3.225182	2.95517	-0.77249	16.26021
<b>0.0259</b>	158.171	3.188876	3.205345	3.224699	2.949492	-0.77237	16.30191
<b>0.0368</b>	158.161	3.188793	3.204526	3.224062	2.942536	-0.77207	16.35031
<b>0.0525</b>	158.0914	3.188814	3.203614	3.222925	2.931349	-0.77186	16.42522
<b>0.0746</b>	158.0189	3.188839	3.202264	3.22139	2.916536	-0.77203	16.52653
<b>0.0928</b>	157.9442	3.188883	3.201589	3.220359	2.907326	-0.77192	16.58269
<b>0.1053</b>	157.946	3.188861	3.200642	3.219423	2.900458	-0.77165	16.62962
<b>0.1234</b>	157.8722	3.188865	3.199676	3.218584	2.890662	-0.77131	16.70087
<b>0.1414</b>	157.8064	3.18887	3.198585	3.217279	2.879254	-0.77107	16.77728
<b>0.1659</b>	157.7161	3.188866	3.197197	3.21537	2.864104	-0.77016	16.88414
<b>0.236</b>	157.4868	3.188785	3.19345	3.210936	2.827205	-0.76990	17.15686
<b>0.2977</b>	157.2632	3.188675	3.19038	3.20701	2.797149	-0.77086	17.38496
<b>0.3934</b>	156.9954	3.188082	3.185162	3.200705	2.755883	-0.77248	17.72018
<b>0.4831</b>	156.7842	3.187391	3.180165	3.19515	2.721692	-0.77495	18.02232
<b>0.5888</b>	156.5197	3.186379	3.174538	3.188543	2.686233	-0.7783	18.34094
<b>0.7054</b>	156.0185	3.185185	3.16887	3.181604	2.654936	-0.78188	18.64073

**Table 5.5.** Absolute values of the DFT calculated equatorial and axial bond length  $d(Pb-X)$ , bond angle  $Pb-X-Pb$ , distance from the nitrogen of each organic spacer to the X plane  $d(N\cdots n_X)$ , titing angle between the organic spacer the  $Pb-X$  plane  $\phi(N\cdots Pb-X)$  and the distance between the spacer  $d(BN\cdots BN)$  for  $(BN)_2PbBr_4$  as a function of pressure.

<i>Pressure</i> (GPa)	<i>Pb-X- Pb</i> (°)	<i>Pb-X-Pb</i> (°)	<i>d(Pb- X)<sub>ax</sub></i> (Å)	<i>d(Pb- X)<sub>eq</sub></i> (Å)	<i>d(Pb- X)<sub>eq</sub></i> (Å)	<i>d(BN- BN)</i> (Å)	<i>d(N<math>\cdots</math>n<sub>X</sub>)</i> (Å)	<i><math>\phi(N\cdots Pb- X)</math></i> (°)
<b>0.0143</b>	141.305	154.31	3.001	2.976	3.018	4.4130		11.88
<b>0.0425</b>	141.251	154.288	3.0011	2.974	3.017	4.3856	-0.4730	12.00
<b>0.07</b>	141.157	154.256	3.0013	2.9724	3.0159	4.3545	-0.4741	12.169
<b>0.086</b>	141.111	154.252	3.0012	2.9712	3.0152	4.3334	-0.4751	12.274
<b>0.1075</b>	141.053	154.250	3.0012	2.9697	3.0143	4.3105	-0.4764	12.375
<b>0.131</b>	141.025	154.231	3.0012	2.9681	3.0134	4.2842	-0.4783	12.499
<b>0.1461</b>	141.068	154.27	3.0007	2.9671	3.0133	4.2598	-0.4814	12.596
<b>0.1639</b>	141.163	154.300	3.0002	2.9659	3.0131	4.2268	-0.4857	12.710
<b>0.1712</b>	141.426	154.414	2.9989	2.9643	3.0135	4.1682	-0.4954	12.887
<b>0.1978</b>	141.414	154.424	2.9962	2.9604	3.0129	4.0554	-0.5185	13.188
<b>0.2128</b>	142.933	154.782	2.9956	2.9582	3.0091	3.9898	-0.5317	12.310
<b>0.2419</b>	144.009	154.701	2.9971	2.9574	2.9993	3.9142	-0.5355	10.327
<b>0.2772</b>	144.538	154.704	2.9972	2.9567	2.9955	3.8591	-0.5392	9.8109
<b>0.311</b>	144.794	154.688	2.9972	2.9547	2.9923	3.8235	-0.5426	9.5804
<b>0.3666</b>	144.994	154.662	2.9971	2.9515	2.9888	3.7783	-0.5474	9.5743
<b>0.4202</b>	145.140	154.619	2.9971	2.9481	2.9853	3.7400	-0.5517	9.5202
<b>0.5322</b>	145.244	154.575	2.9969	2.9410	2.9791	3.6656	-0.560	9.9320

**Table 5.6.** Excitonic peak position and shift obtained from the pressure-dependent optical measurements of (PDMA)PbI<sub>4</sub> by tracking the maximum position of the excitonic peak and by fitting the curve to a skewed Gaussian.

Pressure (GPa)	Max position		Fit	
	Peak energy (eV)	Energy shift (meV)	Peak energy (eV)	Energy shift (meV)
<b>0</b>	2.424±0.002	0	2.4126±0.0002	0
<b>0.10</b>	2.417±0.002	-7.08±3.44	2.406±0.0002	-6.64±0.37
<b>0.15</b>	2.414±0.002	-9.44±3.44	2.401±0.0002	-10.94±0.38
<b>0.20</b>	2.411±0.002	-14.13±3.44	2.397±0.0004	-14.78±0.41
<b>0.25</b>	2.403±0.002	-21.14±3.44	2.391±0.0004	-20.66±0.54
<b>0.30</b>	2.401±0.002	-23.46±3.44	2.388±0.0003	-24.61±0.56
<b>0.35</b>	2.396±0.002	-28.10±3.44	2.385±0.0003	-26.82±0.51

**Table 5.7.** Excitonic peak position and shift obtained from the pressure-dependent optical measurements of (PDMA)PbBr<sub>4</sub> by tracking the maximum position of the excitonic peak and by fitting the curve to a skewed Gaussian.

Pressure (GPa)	Max position		Fit	
	Peak energy (eV)	Energy shift (meV)	Peak energy (eV)	Energy shift (meV)
<b>0</b>	3.092±0.002	0	3.0673±0.0006	0
<b>0.10</b>	3.084±0.002	-7.69±3.44	3.0599±0.0006	-7.38±1.24
<b>0.15</b>	3.081±0.002	-11.52±3.44	3.0551±0.0005	-12.20±1.17
<b>0.20</b>	3.077±0.002	-15.34±3.44	3.0504±0.0005	-16.89±1.17
<b>0.25</b>	3.069±0.002	-22.96±3.44	3.0463±0.0006	-20.94±1.24
<b>0.30</b>	3.069±0.002	-22.96±3.44	3.0420±0.0005	-25.30±1.15
<b>0.35</b>	3.065±0.002	-26.75±3.44	3.0363±0.0003	-31.02±1.03

**Table 5.8.** Excitonic peak position and shift obtained from the pressure-dependent optical measurements of (BN)<sub>2</sub>PbI<sub>4</sub> by tracking the maximum position of the excitonic peak and by fitting the curve to a skewed Gaussian.

Pressure (GPa)	Max position		Fit	
	Peak energy (eV)	Energy shift (meV)	Peak energy (eV)	Energy shift (meV)
<b>0</b>	2.373±0.002	0	2.3668±0.0007	0
<b>0.10</b>	2.364±0.002	-9.04±3.44	2.3596±0.0005	-7.17±1.25
<b>0.15</b>	2.359±0.002	-13.54±3.44	2.3556±0.0004	-11.16±1.16
<b>0.20</b>	2.355±0.002	-18.03±3.44	2.3511±0.0004	-15.66±1.07
<b>0.25</b>	2.348±0.002	-24.72±3.44	2.3455±0.0001	-21.28±0.82
<b>0.30</b>	2.344±0.002	-29.16±3.44	2.3402±0.0003	-26.63±1.01
<b>0.35</b>	2.337±0.002	-35.78±3.44	2.3335±0.0003	-33.29±1.05

**Table 5.9.** Excitonic peak position and shift obtained from the pressure-dependent optical measurements of  $(\text{BN})_2\text{PbBr}_4$  by tracking the maximum position of the excitonic peak and by fitting the curve to a skewed Gaussian.

Pressure (GPa)	Max position		Fit	
	Peak energy (eV)	Energy shift (meV)	Peak energy (eV)	Energy shift (meV)
<b>0</b>	3.103±0.002	0	3.0734±0.0001	0
<b>0.10</b>	3.092±0.002	-11.61±3.44	3.0623±0.0001	-11.15±0.19
<b>0.15</b>	3.084±0.002	-19.30±3.44	3.0535±0.0001	-19.91±0.18
<b>0.20</b>	3.076±0.002	-26.95±3.44	3.0436±0.0001	-29.83±0.17
<b>0.25</b>	3.065±0.002	-38.36±3.44	3.0334±0.0001	-40.03±0.16
<b>0.30</b>	3.057±0.002	-45.92±3.44	3.0355±0.0001	-47.94±0.16
<b>0.35</b>	3.050±0.002	-53.44±3.44	3.0186±0.0001	-54.88±0.17

**Table 5.10.** Computed  $E_{\text{gap}}$  for  $(\text{PDMA})\text{PbI}_4$

Pressure (GPa)	Bandgap (eV)
0.1598	2.1277
0.1621	2.1272
0.1636	2.1264
0.1711	2.1254
0.1797	2.1243
0.1887	2.1235
0.2106	2.1223
0.2168	2.1213
0.2292	2.1202
0.2299	2.1185
0.2459	2.1187
0.2772	2.116
0.2751	2.1143
0.2975	2.1121
0.3142	2.1096
0.3351	2.1068
0.3934	2.1038
0.4299	2.1003
0.5085	2.0957
0.5511	2.0902
0.5994	2.0874
0.6734	2.0824
0.7881	2.078

**Table 5.11.** Computed  $E_{\text{gap}}$  for (PDMA)PbBr<sub>4</sub>

Pressure (GPa)	Bandgap (eV)
0.0042	2.5925
0.0756	2.5828
0.1146	2.5784
0.1427	2.575
0.1686	2.5713
0.1873	2.5696
0.2044	2.5676
0.2184	2.563
0.2335	2.563
0.2404	2.5623
0.2504	2.5613
0.2566	2.5601
0.2623	2.5591
0.269	2.5586
0.2704	2.5577
0.2758	2.5569
0.2819	2.5561
0.2933	2.5553
0.2955	2.555
0.2979	2.5543

**Table 5.12.** Computed  $E_{\text{gap}}$  for (BN)<sub>2</sub>PbBr<sub>4</sub>

Pressure (GPa)	Bandgap (eV)
0.0143	2.7044
0.0425	2.7034
0.07	2.7028
0.086	2.7023
0.1075	2.701
0.131	2.6998
0.1461	2.6969
0.1639	2.6931
0.1712	2.6837
0.1978	2.6576
0.2128	2.6401
0.2419	2.6203
0.2772	2.6091
0.311	2.6008
0.3666	2.5913
0.4202	2.582
0.5322	2.5681
0.6733	2.5547

## 5 - Pressure effects on 2D Perovskites

**Table 5.13.** Computed  $E_{\text{gap}}$  for  $(\text{BN})_2\text{PbI}_4$

Pressure (GPa)	Bandgap (eV)
0	1.9504
0.0259	1.9506
0.0368	1.9501
0.0525	1.9501
0.0746	1.9495
0.0928	1.9497
0.1053	1.9488
0.1234	1.9486
0.1414	1.9483
0.1659	1.9481
0.2128	1.9469
0.3934	1.9462
0.4831	1.9434
0.5888	1.9399
0.7054	1.9359
0.8229	1.9316

### 5.6.3. DETAILED ANALYSIS OF PRESSURE-DEPENDENT XRD

The refinement revealed presence of unreacted substrates in all four mechanosynthesized samples (**Figure A5.8**).

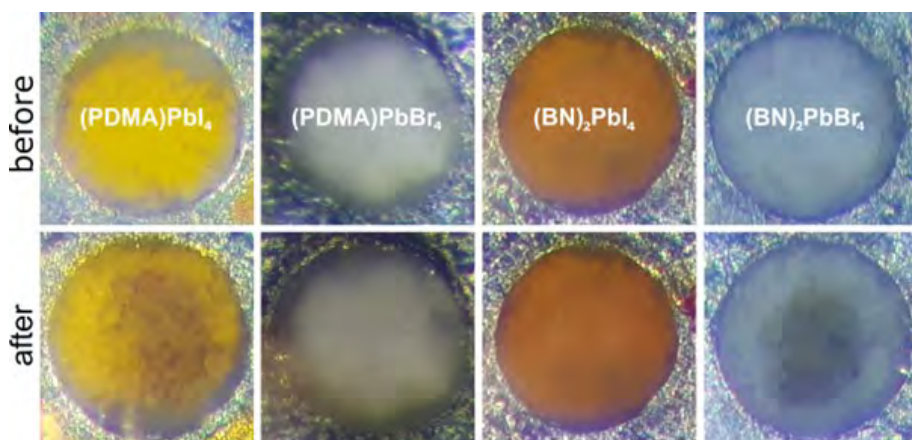


**Figure A5.8.** The samples inside a diamond anvil cell with a visible radiation damage after the experiments.

A detailed description of the XRD patterns for all the four samples (**Figure A5.9**) is reported below. The mechanosynthesis of  $(\text{BN})_2\text{PbI}_4$  resulted in almost a full conversion of the precursors into the desired product. The fitting of  $\text{SiO}_2$  (green) and  $(\text{BN})_2\text{PbI}_4$  (red) patterns left just a few unidentified Bragg peaks (grey plot), which were not assigned neither to  $\text{PbI}_2$  nor  $\text{BN-I}$ . The reaction leading to  $(\text{BN})_2\text{PbBr}_4$  is slower and apart from the product identified (35.9%), the sample contains unreacted precursor  $\text{BN-Br}$  and  $\text{PbBr}_2$  (18.4 and 11.5%, respectively) and the remaining 34.2% is quartz. All significant reflections were fitted during the refinement (grey). The scattering of  $(\text{PDMA})\text{PbI}_4$  sample was weaker, thus no strong high-angle reflections appeared for  $2\theta > 26^\circ$ . Only the product and quartz were identified, but some remaining Bragg peaks (grey) could come from the phases. Although the fitting of full substrate's patterns was unsuccessful, some of the reflections matched, which shows partial amorphization and/or preferential orientation of the substrate crystals after mechanosynthesis. The reaction yield of  $(\text{PDMA})\text{PbBr}_4$  within the given

## 5 - Pressure effects on 2D Perovskites

conversion time is not full as  $\text{PbBr}_2$  (28.8%) and PDMA-Br (18.6%) were identified in the mixture together with the product (21.7%) and the pressure sensor (30.9%). As indicated before, lack of some reflection (*e.g.* 001  $2\theta \sim 3.7^\circ$ ) may suggest preferential orientation of PDMA-Br crystals. On the other hand, no distinguishable Bragg peaks for  $2\theta > 12^\circ$  and broad reflections below may indicate partial amorphisation of the organic precursor. The crystal structure of  $(\text{PDMA})\text{PbBr}_4$  is unknown and for the research purposes it was assumed isostructural to the I-analogue, which gave good agreement with collected data. Attempts to obtain a single crystal confirming the crystal structure were unsuccessful.

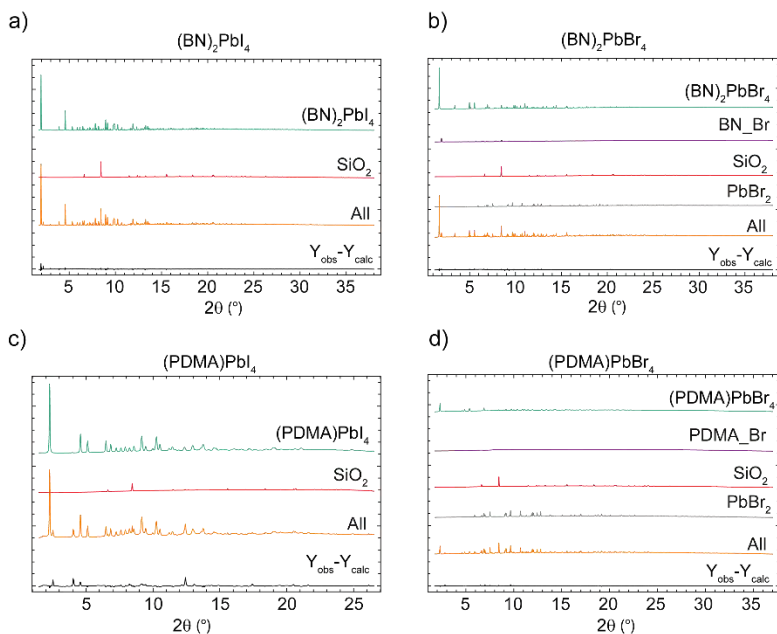


**Figure A5.9.** XRD patterns of **a)**  $(\text{BN})_2\text{PbI}_4$ , **b)**  $(\text{BN})_2\text{PbBr}_4$ , **c)**  $(\text{PDMA})\text{PbI}_4$  and **d)**  $(\text{PDMA})\text{PbBr}_4$  showing the mixtures (orange) and separated patterns of the components, quartz (red), products (green) and unreacted substrates (if present, gray and magenta).

### 5.6.4. BULK MODULUS CALCULATION

Given the mostly isotropic response to the exertion of pressure, we calculate the isothermal bulk modulus from the pressure-volume ( $P$ - $V$ ) relationship (**Figure A5.10**) using the second order Birch-Murnaghan equation of state<sup>43</sup>

$$P = \frac{3}{2} K_{T0} \left[ \left( \frac{V_0}{V} \right)^{\frac{7}{3}} - \left( \frac{V_0}{V} \right)^{\frac{5}{3}} \right] \quad (5.1)$$

where  $K_{T0}$  is the isothermal bulk modulus at standard temperature,  $V_0$  is the initial volume,  $V$  is the volume at pressure  $P$ . To account for the isostructural phase transition in  $(\text{BN})_2\text{PbBr}_4$ , the two-phase transition regimes are fitted separately and two  $K_{T0}$  are obtained for this composition (**Table 5.14**).

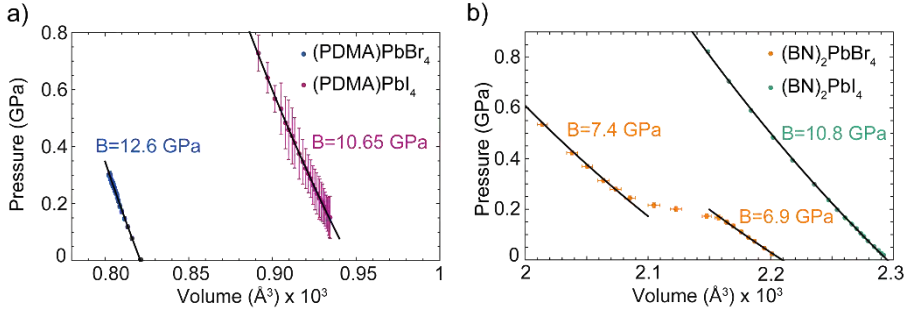


**Figure A5.10.** Pressure-Volume ( $P$ - $V$ ) relationship as a function of pressure fitted with second order Birch-Murnaghan equation of state fit (solid black line) for **a)**  $(\text{PDMA})\text{PbX}_4$  and **b)**  $(\text{BN})_2\text{PbX}_4$ . Here,  $c$ -axis is the out-of-plane direction and  $a$  and  $b$  axis are the in-plane ones.

**Table 5.14.** Isothermal bulk moduli for the layered 2D perovskites studied.

Composition	$K_{T0}$ (GPa)
$(\text{PDMA})\text{PbI}_4$	$10.65 \pm 0.06$
$(\text{PDMA})\text{PbBr}_4$	$12.6 \pm 0.1$
$(\text{BN})_2\text{PbI}_4$	$10.88 \pm 0.03$
$(\text{BN})_2\text{PbBr}_4$ ( $< 0.14$ GPa)	$6.9 \pm 0.1$
$(\text{BN})_2\text{PbBr}_4$ ( $> 0.14$ GPa)	$7.4 \pm 0.2$

## 5 - Pressure effects on 2D Perovskites

A larger bulk modulus suggests a greater stiffness of the material. While one might expect that RP-type layered perovskites should be less rigid and more compressible due to van der Waals interactions in the spacer bilayers, the bulk modulus of (BN)PbI<sub>4</sub> is comparable to (PDMA)PbI<sub>4</sub>. However, the behaviour of the bromide analogues is different; (BN)<sub>2</sub>PbBr<sub>4</sub> shows a significantly smaller bulk modulus indicating higher compressibility and pressure responsiveness. According to the obtained bulk modulus, we expect a more pronounced effect of the pressure to the optoelectronic properties in the case of (BN)<sub>2</sub>PbBr<sub>4</sub>.

## 5.7. References

- (1) Saparov, B.; Mitzi, D. B. Organic – Inorganic Perovskites: Structural Versatility for Functional Materials Design. *Chem. Rev.* **2016**, *116* (7). <https://doi.org/10.1021/acs.chemrev.5b00715>.
- (2) Grancini, G.; Nazeeruddin, M. K. Dimensional Tailoring of Hybrid Perovskites for Photovoltaics. *Nat. Rev. Mater.* **2019**, *4* (1). <https://doi.org/10.1038/s41578-018-0065-0>.
- (3) Blancon, J. C.; Even, J.; Stoumpos, C. C.; Kanatzidis, M. G.; Mohite, A. D. Semiconductor Physics of Organic–Inorganic 2D Halide Perovskites. *Nat. Nanotechnol.* **2020**, *15* (12). <https://doi.org/10.1038/s41565-020-00811-1>.
- (4) Li, X.; Hoffman, J. M.; Kanatzidis, M. G. The 2D Halide Perovskite Rulebook: How the Spacer Influences Everything from the Structure to Optoelectronic Device Efficiency. *Chem. Rev.* **2021**, *121* (4). <https://doi.org/10.1021/acs.chemrev.0c01006>.
- (5) Stoumpos, C. C.; Cao, D. H.; Clark, D. J.; Young, J.; Rondinelli, J. M.; Jang, J. I.; Hupp, J. T.; Kanatzidis, M. G. Ruddlesden – Popper Hybrid Lead Iodide Perovskite 2D Homologous Semiconductors. *Chem. Mater.* **2016**, *28*. <https://doi.org/10.1021/acs.chemmater.6b00847>.
- (6) Mao, L.; Ke, W.; Pedesseau, L.; Wu, Y.; Katan, C.; Even, J.; Wasielewski, M. R.; Stoumpos, C. C.; Kanatzidis, M. G. Hybrid Dion–Jacobson 2D Lead Iodide Perovskites. *J. Am. Chem. Soc.* **2018**, *140*. <https://doi.org/10.1021/jacs.8b00542>.
- (7) Kong, L.; Liu, G.; Gong, J.; Mao, L.; Chen, M.; Hu, Q.; Lü, X.; Yang, W.; Kanatzidis, M. G.; Mao, H. K. Highly Tunable Properties in Pressure-Treated Two-Dimensional Dion–Jacobson Perovskites. *Proc. Natl. Acad. Sci. U. S. A.* **2020**, *117* (28). <https://doi.org/10.1073/pnas.2003561117>.
- (8) Mao, L.; Stoumpos, C. C.; Kanatzidis, M. G. Two-Dimensional Hybrid Halide Perovskites: Principles and Promises. *J. Am. Chem. Soc.* **2018**, *141* (3). <https://doi.org/10.1021/JACS.8B10851>.
- (9) Blancon, J.; Stier, A. V; Tsai, H.; Nie, W.; Stoumpos, C. C.; Traoré, B.; Pedesseau, L.; Kepenekian, M.; Katsutani, F.; Noe, G. T.; et al. Scaling Law for Excitons in 2D Perovskite Quantum Wells. *Nat. Commun.* **2018**, *9*. <https://doi.org/10.1038/s41467-018-04659-x>.
- (10) Sichert, J. A.; Hemmerling, A.; Cardenas-Daw, C.; Urban, A. S.; Feldmann, J. Tuning the Optical Bandgap in Layered Hybrid Perovskites through Variation of Alkyl Chain Length. *APL Mater.* **2019**, *7* (4).

<https://doi.org/10.1063/1.5087296>.

- (11) Zhang, K.; Zhang, M.; Zhu, N.; Yin, H.; Xing, J.; Wang, L. Effects of Organic Ligands on Efficiency and Stability of Perovskite Light-Emitting Diodes. *J. Mater. Sci.* **2021**, *56* (19). <https://doi.org/10.1007/s10853-021-06022-w>.
- (12) Jaffe, A.; Lin, Y.; Karunadasa, H. I. Halide Perovskites under Pressure: Accessing New Properties through Lattice Compression. *ACS Energy Lett.* **2017**, *2* (7). <https://doi.org/10.1021/acseenergylett.7b00284>.
- (13) Liu, S.; Sun, S.; Gan, C. K.; Del Águila, A. G.; Fang, Y.; Xing, J.; Thu Ha Do, T.; White, T. J.; Li, H.; Huang, W.; et al. Manipulating Efficient Light Emission in Two-Dimensional Perovskite Crystals by Pressure-Induced Anisotropic Deformation. *Sci. Adv.* **2019**, *5* (7). <https://doi.org/10.1126/sciadv.aav9445>.
- (14) Jaffe, A.; Lin, Y.; Beavers, C. M.; Voss, J.; Mao, W. L.; Karunadasa, H. I. High-Pressure Single-Crystal Structures of 3D Lead-Halide Hybrid Perovskites and Pressure Effects on Their Electronic and Optical Properties. *ACS Cent. Sci.* **2016**, *2* (4). <https://doi.org/10.1021/acscentsci.6b00055>.
- (15) Szafranski, M.; Katrusiak, A. Photovoltaic Hybrid Perovskites under Pressure. *J. Phys. Chem. Lett.* **2017**, *8* (11). <https://doi.org/10.1021/acs.jpcllett.7b00520>.
- (16) Jaffe, A.; Lin, Y.; L. Mao, W.; I. Karunadasa, H. Pressure-Induced Conductivity and Yellow-to-Black Piezochromism in a Layered Cu–Cl Hybrid Perovskite. *J. Am. Chem. Soc.* **2015**, *137* (4). <https://doi.org/10.1021/ja512396m>.
- (17) Umeyama, D.; Lin, Y.; I. Karunadasa, H. Red-to-Black Piezochromism in a Compressible Pb–I–SCN Layered Perovskite. *Chem. Mater.* **2016**, *28* (10). <https://doi.org/10.1021/acs.chemmater.6b01147>.
- (18) Li, Q.; Yin, L.; Chen, Z.; Deng, K.; Luo, S.; Zou, B.; Wang, Z.; Tang, J.; Quan, Z. High Pressure Structural and Optical Properties of Two-Dimensional Hybrid Halide Perovskite (CH<sub>3</sub>NH<sub>3</sub>)<sub>3</sub>Bi<sub>2</sub>Br<sub>9</sub>. *Inorg. Chem.* **2019**, *58* (2). <https://doi.org/10.1021/acs.inorgchem.8b03190>.
- (19) Mao, H. K.; Chen, L. C.; Hemley, R. J.; Jephcoat, A. P.; Wu, Y.; Bassett, W. A. Stability and Equation of State of CaSiO<sub>3</sub>-Perovskite to 134 GPa. *J. Geophys. Res. Solid Earth* **1989**, *94* (B12). <https://doi.org/https://doi.org/10.1029/JB094iB12p17889>.
- (20) Kung, J.; Rigden, S. Oxide Perovskites: Pressure Derivatives of the Bulk and Shear Moduli. *Phys. Chem. Miner.* **1999**, *26* (3). <https://doi.org/10.1007/s002690050182>.

- (21) Liu, G.; Gong, J.; Kong, L.; Schaller, R. D.; Hu, Q.; Liu, Z.; Yan, S.; Yang, W.; Stoumpos, C. C.; Kanatzidis, M. G.; et al. Isothermal Pressure-Derived Metastable States in 2D Hybrid Perovskites Showing Enduring Bandgap Narrowing. *Proc. Natl. Acad. Sci. U. S. A.* **2018**, *115* (32). <https://doi.org/10.1073/pnas.1809167115>.
- (22) Liu, S.; Sun, S.; Kwan Gan, C.; Granados del Águila, A.; Fang, Y.; Xing, J.; Thu Ha Do, T.; White, T. J.; Li, H.; Huang, W.; et al. Manipulating Efficient Light Emission in Two-Dimensional Perovskite Crystals by Pressure-Induced Anisotropic Deformation. *Sci. Adv.* **2019**, *5* (7). <https://doi.org/10.1126/sciadv.aav9445>.
- (23) Tu, Q.; Spanopoulos, I.; Yasaei, P.; Stoumpos, C. C.; Kanatzidis, M. G.; Shekhawat, G. S.; Dravid, V. P. Stretching and Breaking of Ultrathin 2D Hybrid Organic-Inorganic Perovskites. *ACS Nano* **2018**, *12* (10). <https://doi.org/10.1021/acsnano.8b05623>.
- (24) Tu, Q.; Spanopoulos, I.; Hao, S.; Wolverton, C.; Kanatzidis, M. G.; Shekhawat, G. S.; Dravid, V. P. Out-of-Plane Mechanical Properties of 2D Hybrid Organic-Inorganic Perovskites by Nanoindentation. *ACS Appl. Mater. Interfaces* **2018**, *10* (26). <https://doi.org/10.1021/acsmi.8b05138>.
- (25) Tu, Q.; Spanopoulos, I.; Vasileiadou, E. S.; Li, X.; Kanatzidis, M. G.; Shekhawat, G. S.; Dravid, V. P. Exploring the Factors Affecting the Mechanical Properties of 2D Hybrid Organic-Inorganic Perovskites. *ACS Appl. Mater. Interfaces* **2020**, *12* (18). <https://doi.org/10.1021/acsmi.0c02313>.
- (26) Liu, G.; Kong, L.; Guo, P.; Stoumpos, C. C.; Hu, Q.; Liu, Z.; Cai, Z.; Gosztola, D. J.; Mao, H. K.; Kanatzidis, M. G.; et al. Two Regimes of Bandgap Red Shift and Partial Ambient Retention in Pressure-Treated Two-Dimensional Perovskites. *ACS Energy Lett.* **2017**, *2* (11). <https://doi.org/10.1021/acsenerylett.7b00807>.
- (27) Du, K.-Z. Z.; Tu, Q.; Zhang, X.; Han, Q.; Liu, J.; Zauscher, S.; Mitzi, D. B. Two-Dimensional Lead(II) Halide-Based Hybrid Perovskites Templated by Acene Alkylamines: Crystal Structures, Optical Properties, and Piezoelectricity. *Inorg. Chem.* **2017**, *56* (15). <https://doi.org/10.1021/acs.inorgchem.7b01094>.
- (28) Kong, L.; Liu, G.; Gong, J.; Hu, Q.; Schaller, R. D.; Dera, P.; Zhang, D.; Liu, Z.; Yang, W.; Zhu, K.; et al. Simultaneous Band-Gap Narrowing and Carrier-Lifetime Prolongation of Organic-Inorganic Trihalide Perovskites. *Proc. Natl. Acad. Sci. U. S. A.* **2016**, *113* (32). <https://doi.org/10.1073/pnas.1609030113>.
- (29) Guzelturk, B.; Winkler, T.; Van de Goor, T. W. J.; Smith, M. D.; Bourelle, S. A.; Feldmann, S.; Trigo, M.; Teitelbaum, S. W.; Steinrück, H. G.; de la

- Pena, G. A.; et al. Visualization of Dynamic Polaronic Strain Fields in Hybrid Lead Halide Perovskites. *Nat. Mater.* **2021**, *20* (5). <https://doi.org/10.1038/s41563-020-00865-5>.
- (30) Limmer, D. T.; Ginsberg, N. S. Photoinduced Phase Separation in the Lead Halides Is a Polaronic Effect. *J. Chem. Phys.* **2020**, *152* (23). <https://doi.org/10.1063/1.5144291>.
- (31) Zhu, C.; Niu, X.; Fu, Y.; Li, N.; Hu, C.; Chen, Y.; He, X.; Na, G.; Liu, P.; Zai, H.; et al. Strain Engineering in Perovskite Solar Cells and Its Impacts on Carrier Dynamics. *Nat. Commun.* **2019**, *10* (1). <https://doi.org/10.1038/s41467-019-08507-4>.
- (32) Liu, D.; Luo, D.; Iqbal, A. N.; Orr, K. W. P.; Doherty, T. A. S.; Lu, Z. H.; Stranks, S. D.; Zhang, W. Strain Analysis and Engineering in Halide Perovskite Photovoltaics. *Nature Materials.* **2021**, *20* (10). <https://doi.org/10.1038/s41563-021-01097-x>.
- (33) Chen, Y.; Lei, Y.; Li, Y.; Yu, Y.; Cai, J.; Chiu, M. H.; Rao, R.; Gu, Y.; Wang, C.; Choi, W.; et al. Strain Engineering and Epitaxial Stabilization of Halide Perovskites. *Nature* **2020**, *577* (7789). <https://doi.org/10.1038/s41586-019-1868-x>.
- (34) Zhang, C.; Wu, S.; Tao, L.; Arumugam, G. M.; Liu, C.; Wang, Z.; Zhu, S.; Yang, Y.; Lin, J.; Liu, X.; et al. Fabrication Strategy for Efficient 2D/3D Perovskite Solar Cells Enabled by Diffusion Passivation and Strain Compensation. *Adv. Energy Mater.* **2020**, *10* (43). <https://doi.org/10.1002/aenm.202002004>.
- (35) Gélvez-Rueda, M. C.; Ahlawat, P.; Merten, L.; Jahanbakhshi, F.; Mladenović, M.; Hinderhofer, A.; Dar, M. I.; Li, Y.; Dučinskas, A.; Carlsen, B.; et al. Formamidinium-Based Dion-Jacobson Layered Hybrid Perovskites: Structural Complexity and Optoelectronic Properties. *Adv. Funct. Mater.* **2020**, *30* (38). <https://doi.org/10.1002/adfm.202003428>.
- (36) Yu, S.; Yan, Y.; Abdellah, M.; Pullerits, T.; Zheng, K.; Liang, Z. Nonconfinement Structure Revealed in Dion–Jacobson Type Quasi-2D Perovskite Expedites Interlayer Charge Transport. *Small* **2019**, *15* (49). <https://doi.org/10.1002/sml.201905081>.
- (37) Kamminga, M. E.; Fang, H.-H. H.; Filip, M. R.; Giustino, F.; Baas, J.; Blake, G. R.; Loi, M. A.; Palstra, T. T. M. M. Confinement Effects in Low-Dimensional Lead Iodide Perovskite Hybrids. *Chem. Mater.* **2016**, *28* (13). <https://doi.org/10.1021/acs.chemmater.6b00809>.
- (38) Li, Y.; Milić, J. V.; Ummadisingu, A.; Seo, J. Y.; Im, J. H.; Kim, H. S.; Liu, Y.; Dar, M. I.; Zakeeruddin, S. M.; Wang, P.; et al. Bifunctional Organic Spacers for Formamidinium-Based Hybrid Dion-Jacobson Two-Dimensional Perovskite Solar Cells. *Nano Lett.* **2019**, *19* (1).

<https://doi.org/10.1021/acs.nanolett.8b03552>.

- (39) Kamminga, M. E.; Fang, H.-H.; Filip, M. R.; Giustino, F.; Baas, J.; Blake, G. R.; Loi, M. A.; Palstra, T. T. M. Confinement Effects in Low-Dimensional Lead Iodide Perovskite Hybrids. *Chem. Mater* **2016**, *28*, 2. <https://doi.org/10.1021/acs.chemmater.6b00809>.
- (40) Mao, L.; Ke, W.; Pedesseau, L.; Wu, Y.; Katan, C.; Even, J.; Wasielewski, M. R.; Stoumpos, C. C.; Kanatzidis, M. G. Hybrid Dion–Jacobson 2D Lead Iodide Perovskites  $\text{Sn I } 3n+1$  ( $n = 2-3$ ),  $(\text{CH}_3\text{C}_6\text{H}_4\text{CH}_2\text{NH}_3)_2$  (MA) $\text{Pb}_2\text{I}_7$ ,  $(\text{HO}_2\text{C}(\text{CH}_2)_3\text{NH}_3)_2(\text{MA})\text{PbI}_7$ ,  $(\text{C}_4\text{H}_3\text{SCH}_2\text{NH}_3)_2(\text{MA})\text{Pb}_2\text{I}_7$ ,  $(\text{EA})_4\text{Pb}_3\text{X}_{10}$  ( $\text{X} = \text{Cl}$ ). *J. Am. Chem. Soc* **2018**, *140*, 47. <https://doi.org/10.1021/jacs.8b00542>.
- (41) Du, K.-Z.; Tu, Q.; Zhang, X.; Han, Q.; Liu, J.; Zauscher, S.; Mitzi, D. B. Two-Dimensional Lead(II) Halide-Based Hybrid Perovskites Templated by Acene Alkylamines: Crystal Structures, Optical Properties, and Piezoelectricity. *Inorg. Chem* **2017**, *56*, 28. <https://doi.org/10.1021/acs.inorgchem.7b01094>.
- (42) Wang, L.; Wang, K.; Xiao, G.; Zeng, Q.; Zou, B. Pressure-Induced Structural Evolution and Band Gap Shifts of Organometal Halide Perovskite-Based Methylammonium Lead Chloride. *J. Phys. Chem. Lett.* **2016**, *7* (24). <https://doi.org/10.1021/acs.jpcclett.6b02420>.
- (43) Katsura, T.; Tange, Y. A Simple Derivation of the Birch–Murnaghan Equations of State (EOSs) and Comparison with EOSs Derived from Other Definitions of Finite Strain. *Minerals* **2019**, *9* (12). <https://doi.org/10.3390/min9120745>.
- (44) Liang, A.; Rahman, S.; Saqib, H.; Rodriguez-Hernandez, P.; Muñoz, A.; Nénert, G.; Yousef, I.; Popescu, C.; Errandonea, D. First-Order Isostructural Phase Transition Induced by High Pressure in  $\text{Fe}(\text{IO}_3)_3$ . *J. Phys. Chem. C* **2020**, *124* (16). <https://doi.org/10.1021/acs.jpcc.0c02080>.
- (45) Kitazawa, N. Excitons in Two-Dimensional Layered Perovskite Compounds:  $(\text{C}_6\text{H}_5\text{C}_2\text{H}_4\text{NH}_3)_2\text{Pb}(\text{Br},\text{I})_4$  and  $(\text{C}_6\text{H}_5\text{C}_2\text{H}_4\text{NH}_3)_2\text{Pb}(\text{Cl},\text{Br})_4$ . *Mater. Sci. Eng. B* **1997**, *49* (3). [https://doi.org/10.1016/S0921-5107\(97\)00132-3](https://doi.org/10.1016/S0921-5107(97)00132-3).
- (46) Hong, X.; Ishihara, T.; Nurmikko, A. V. Dielectric Confinement Effect on Excitons in  $\text{PbI}_4$ -Based Layered Semiconductors, **1992**. <https://doi.org/10.1103/PhysRevB.45.6961>.
- (47) Chen, Y.; Fu, R.; Wang, L.; Ma, Z.; Xiao, G.; Wang, K.; Zou, B. Emission Enhancement and Bandgap Retention of a Two-Dimensional Mixed Cation Lead Halide Perovskite under High Pressure. *J. Mater. Chem. A* **2019**, *7* (11). <https://doi.org/10.1039/c8ta11992a>.

- (48) Qin, Y.; Lv, Z.; Chen, S.; Li, W.; Wu, X.; Ye, L.; Li, N.; Lu, P. Tuning Pressure-Induced Phase Transitions, Amorphization, and Excitonic Emissions of 2D Hybrid Perovskites via Varying Organic Amine Cations. *J. Phys. Chem. C* **2019**, *123*, 45. <https://doi.org/10.1021/acs.jpcc.9b06169>.
- (49) Zhang, L.; Wu, L.; Wang, K.; Zou, B. Pressure-Induced Broadband Emission of 2D Organic–Inorganic Hybrid Perovskite (C<sub>6</sub>H<sub>5</sub>C<sub>2</sub>H<sub>4</sub>NH<sub>3</sub>)<sub>2</sub>PbBr<sub>4</sub>. *Adv. Sci.* **2019**, *6* (2). <https://doi.org/10.1002/advs.201801628>.
- (50) Al-Qatatsheh, A.; Morsi, Y.; Zavabeti, A.; Zolfagharian, A.; Salim, N.; Kouzani, A. Z.; Mosadegh, B.; Gharaie, S.; Au, A. Z. K. Blood Pressure Sensors: Materials, Fabrication Methods, Performance Evaluations and Future Perspectives, **2020**, *20* (16). <https://doi.org/10.3390/s20164484>.
- (51) Park, J.; Lee, Y.; Barbee, M. H.; Cho, S.; Cho, S.; Shanker, R.; Kim, J.; Myoung, J.; Kim, M. P.; Baig, C.; et al. A Hierarchical Nanoparticle-in-Micropore Architecture for Enhanced Mechanosensitivity and Stretchability in Mechanochromic Electronic Skins. *Adv. Mater.* **2019**, *31* (25). <https://doi.org/10.1002/adma.201808148>.
- (52) Cho, S.; Kang, S.; Pandya, A.; Shanker, R.; Khan, Z.; Lee, Y.; Park, J.; Craig, S. L.; Ko, H. Large-Area Cross-Aligned Silver Nanowire Electrodes for Flexible, Transparent, and Force-Sensitive Mechanochromic Touch Screens. *ACS Nano* **2017**, *11*, 7. <https://doi.org/10.1021/acs.nano.7b01714>.
- (53) Zhang, W.; Ye, H.-Y.; Graf, R.; Spiess, H. W.; Yao, Y.-F.; Zhu, R.-Q.; Xiong, R.-G. Tunable and Switchable Dielectric Constant in an Amphidynamic Crystal. *J. Am. Chem. Soc.* **2013**, *135*, 7. <https://doi.org/10.1021/ja3110335>.
- (54) Sun, Y. L.; Shi, C.; Zhang, W. Distinct Room-temperature Dielectric Transition in a Perchlorate-Based Organic-Inorganic Hybrid Perovskite. *Dalt. Trans.* **2017**, *46* (48). <https://doi.org/10.1039/c7dt03798h>.
- (55) Giannozzi, P.; Andreussi, O.; Brumme, T.; Bunau, O.; Buongiorno Nardelli, M.; Calandra, M.; Car, R.; Cavazzoni, C.; Ceresoli, D.; Cococcioni, M.; et al. Advanced Capabilities for Materials Modelling with Quantum ESPRESSO. *J. Phys. Condens. Matter* **2017**, *29* (46). <https://doi.org/10.1088/1361-648X/aa8f79>.
- (56) Giannozzi, P.; Baseggio, O.; Bonfà, P.; Brunato, D.; Car, R.; Carnimeo, I.; Cavazzoni, C.; De Gironcoli, S.; Delugas, P.; Ferrari Ruffino, F.; et al. Quantum ESPRESSO toward the Exascale. *J. Chem. Phys.* **2020**, *152* (15). <https://doi.org/10.1063/5.0005082>.
- (57) Giannozzi, P.; Baroni, S.; Bonini, N.; Calandra, M.; Car, R.; Cavazzoni,

- C.; Ceresoli, D.; Chiarotti, G. L.; Cococcioni, M.; Dabo, I.; et al. QUANTUM ESPRESSO: A Modular and Open-Source Software Project for Quantum Simulations of Materials. *J. Phys. Condens. Matter* **2009**, *21* (39). <https://doi.org/10.1088/0953-8984/21/39/395502>.
- (58) Willmott, P. R.; Meister, D.; Leake, S. J.; Lange, M.; Bergamaschi, A.; Böge, M.; Calvi, M.; Cancellieri, C.; Casati, N.; Cervellino, A.; et al. The Materials Science Beamline Upgrade at the Swiss Light Source. *J. Synchrotron Radiat.* **2013**, *20* (5). <https://doi.org/10.1107/S0909049513018475>.
- (59) Angel, R. J.; Allan, D. R.; Miletich, R.; Finger, L. W. The Use of Quartz as an Internal Pressure Standard in High-Pressure Crystallography. *J. Appl. Crystallogr.* **1997**, *30* (4). <https://doi.org/10.1107/S0021889897000861>.
- (60) Prescher, C.; Prakapenka, V. B. DIOPTAS: A Program for Reduction of Two-Dimensional X-Ray Diffraction Data and Data Exploration. <http://dx.doi.org/10.1080/08957959.2015.1059835> **2015**, *35* (3). <https://doi.org/10.1080/08957959.2015.1059835>.
- (61) Coelho, A. A.; Evans, J.; Evans, I.; Kern, A.; Parsons, S. The TOPAS Symbolic Computation System. *Powder Diffr.* **2011**, *26*. <https://doi.org/10.1154/1.3661087>.
- (62) Rietveld, H. M. A Profile Refinement Method for Nuclear and Magnetic Structures. *J. Appl. Crystallogr.* **1969**, *2* (2). <https://doi.org/10.1107/S0021889869006558>.